

Merging black hole binaries with the SEVN code

Mario Spera^{1,2,3,4,5,6★} Michela Mapelli^{1,2,3,4★} Nicola Giacobbo^{1,2,3}
 Alessandro A. Trani^{3,7,8} Alessandro Bressan^{3,8} and Guglielmo Costa^{1,8}

¹Dipartimento di Fisica e Astronomia ‘G. Galilei’, University of Padova, Vicolo dell’Osservatorio 3, I-35122 Padova, Italy

²INFN, Sezione di Padova, Via Marzolo 8, I-35131 Padova, Italy

³INAF, Osservatorio Astronomico di Padova, Vicolo dell’Osservatorio 5, I-35122 Padova, Italy

⁴Institut für Astro- und Teilchenphysik, Universität Innsbruck, Technikerstrasse 25/8, A-6020, Innsbruck, Austria

⁵Department of Physics and Astronomy, Northwestern University, Evanston, IL 60208, USA

⁶Center for Interdisciplinary Exploration and Research in Astrophysics (CIERA), Evanston, IL 60208, USA

⁷Department of Astronomy, Graduate School of Science, The University of Tokyo, 7-3-1 Hongo, Bunkyo-ku, Tokyo 113-0033, Japan

⁸SISSA, via Bonomea 265, I-34136 Trieste, Italy

Accepted 2019 January 29. Received 2019 January 11; in original form 2018 September 11

ABSTRACT

Studying the formation and evolution of black hole binaries (BHBs) is essential for the interpretation of current and forthcoming gravitational wave (GW) detections. We investigate the statistics of BHBs that form from isolated binaries, by means of a new version of the SEVN population-synthesis code. SEVN integrates stellar evolution by interpolation over a grid of stellar evolution tracks. We upgraded SEVN to include binary stellar evolution processes and we used it to evolve a sample of 1.5×10^8 binary systems, with metallicity in the range $[10^{-4}, 4 \times 10^{-2}]$. From our simulations, we find that the mass distribution of black holes (BHs) in double compact-object binaries is remarkably similar to the one obtained considering only single stellar evolution. The maximum BH mass we obtain is $\sim 30, 45$, and $55 M_{\odot}$ at metallicity $Z = 2 \times 10^{-2}, 6 \times 10^{-3}$, and 10^{-4} , respectively. A few massive single BHs may also form ($\lesssim 0.1$ per cent of the total number of BHs), with mass up to $\sim 65, 90$, and $145 M_{\odot}$ at $Z = 2 \times 10^{-2}, 6 \times 10^{-3}$, and 10^{-4} , respectively. These BHs fall in the mass gap predicted from pair-instability supernovae. We also show that the most massive BHBs are unlikely to merge within a Hubble time. In our simulations, merging BHs like GW151226 and GW170608, form at all metallicities, the high-mass systems (like GW150914, GW170814, and GW170104) originate from metal-poor ($Z \lesssim 6 \times 10^{-3}$) progenitors, whereas GW170729-like systems are hard to form, even at $Z = 10^{-4}$. The BHB merger rate in the local Universe obtained from our simulations is $\sim 90 \text{ Gpc}^{-3} \text{ yr}^{-1}$, consistent with the rate inferred from LIGO–Virgo data.

Key words: black hole physics – gravitational waves – methods: numerical – binaries: general – stars: mass-loss.

1 INTRODUCTION

The existence of double black hole binaries (BHBs) has been hypothesized for several decades (Tutukov, Yungelson & Klayman 1973; Thorne 1987; Schutz 1989; Kulkarni, Hut & McMillan 1993; Sigurdsson & Phinney 1993; Portegies Zwart & McMillan 2000; Colpi, Mapelli & Possenti 2003; Belczynski, Sadowski & Rasio 2004), but their first observational confirmation is the detection of GW150914 in September 2015 (Abbott et al. 2016b). Since then, nine additional BHB mergers have been reported by the LIGO–Virgo collaboration (Aasi et al. 2015; Acernese et al. 2015):

GW151012 (Abbott et al. 2018a), GW151226 (Abbott et al. 2016a), GW170104 (Abbott et al. 2017a), GW170608 (Abbott et al. 2017c), GW170729, GW170809 (Abbott et al. 2018a), GW170814 (Abbott et al. 2017b), GW170818, and GW170823 (Abbott et al. 2018a).

Seven of the observed merging systems host black holes (BHs) with mass larger than $\sim 30 M_{\odot}$. These massive BHs were a surprise for the astrophysics community, because there is no conclusive evidence for BHs with mass $> 20 M_{\odot}$ from X-ray binaries¹ (Özel et al. 2010; Farr et al. 2011).

¹The compact object in the X-ray binary IC10 X-1 was estimated to have a mass of $\sim 28–34 M_{\odot}$ (Prestwich et al. 2007; Silverman & Filippenko 2008), but this result is still debated (Laycock, Maccarone & Christodoulou 2015).

* E-mail: mario.spera@live.it (MS); michela.mapelli@inaf.it (MM)

If these BHs formed from the collapse of massive stars, such large masses require the progenitors to be massive metal-poor stars (Mapelli, Colpi & Zampieri 2009; Mapelli et al. 2010; Belczynski et al. 2010; Mapelli et al. 2013; Mapelli & Zampieri 2014; Spera, Mapelli & Bressan 2015). Massive metal-poor stars are thought to lose less mass by stellar winds than their metal-rich analogues (Vink, de Koter & Lamers 2001; Gräfener & Hamann 2008; Vink et al. 2011). Thus, a metal-poor star ends its life with a larger mass than a metal-rich star with the same zero-age main sequence (ZAMS) mass. Although our knowledge of the hydrodynamics of core-collapse supernovae (SNe) is far from optimal (see Foglizzo et al. 2015 for a recent review), several studies (Fryer 1999; Fryer, Woosley & Heger 2001; Heger et al. 2003; O'Connor & Ott 2011; Fryer et al. 2012; Ugliano et al. 2012; Ertl et al. 2016) suggest that if the mass and/or the compactness of the star at the onset of collapse are sufficiently large, then the star can avoid an SN explosion and collapse to a BH promptly, leading to the formation of a relatively massive BH. Since metal-poor stars lose less mass by stellar winds, they are also more likely to form massive BHs via direct collapse than metal-rich stars (Spera et al. 2015; Belczynski et al. 2016a). Stellar rotation (e.g. Limongi 2017; Limongi & Chieffi 2018), magnetic fields (Petit et al. 2017), pair-instability SNe (PISNe), and pulsational pair-instability SNe (PPISNe) (Belczynski et al. 2016b; Spera & Mapelli 2017; Woosley 2017) also affect this picture.

Other possible scenarios for the formation of $\sim 30\text{--}40 M_{\odot}$ BHs include primordial BHs (i.e. BHs formed by gravitational instabilities in the very early Universe, e.g. Carr, Künnel & Sandstad 2016; Sasaki et al. 2018) and second-generation BHs (i.e. BHs formed from the mergers of smaller stellar BHs, Gerosa & Berti 2017). Stellar dynamics in dense star clusters can also affect the final mass of merging BHs (e.g. Portegies Zwart et al. 2004; Giersz et al. 2015; Mapelli 2016).

Overall, the formation of massive stellar BHs ($30\text{--}40 M_{\odot}$) is still an open question, several aspects of massive star evolution and core-collapse SN explosions being poorly understood.

The formation channels of BHBs are even more debated. A BHB can form from the evolution of massive close stellar binaries (e.g. Tutukov et al. 1973; Bethe & Brown 1998; Belczynski et al. 2016a; de Mink & Mandel 2016; Giacobbo, Mapelli & Spera 2018; Mandel & de Mink 2016; Marchant et al. 2016; Mapelli & Giacobbo 2018) or from dynamical processes involving BHs in dense star clusters (e.g. Portegies Zwart & McMillan 2000; Colpi et al. 2003; Ziosi et al. 2014; Giersz et al. 2015; Askar et al. 2016; Kimpton et al. 2016; Mapelli 2016; Rodriguez et al. 2016; Banerjee 2017). In this manuscript, we will focus on the evolution of a massive close stellar binary ‘isolation’, that is without considering dynamical processes in star clusters.

A large fraction of massive stars ($\sim 50\text{--}70$ per cent, Sana et al. 2012) are members of binary systems since their birth. The evolution of a close stellar binary is affected by a number of physical processes, such as mass transfer (via stellar winds or Roche lobe overflow), common envelope (CE), and tides (e.g. Portegies Zwart & Verbunt 1996; Bethe & Brown 1998; Hurley, Tout & Pols 2002). Thus, the final fate of a binary member can be completely different from that of a single star with the same ZAMS mass and metallicity. This affects the statistics of merging BHBs, because it changes the number of BHBs and their properties (masses, eccentricities, semimajor axes, and spins).

Binary population synthesis codes have been used to study the evolution of massive binaries and their impact for the demography of BHBs. Since the pioneering work by Whyte & Eggleton (1985), several population synthesis codes have been developed. The

‘binary-star evolution’ (BSE) code (Hurley, Pols & Tout 2000; Hurley et al. 2002) is surely one of the most used population synthesis codes. Stellar evolution is implemented in BSE through polynomial fitting formulas, making this code amazingly fast. The fitting formulas adopted in BSE are based on quite outdated stellar evolution models. For this reason, Giacobbo et al. (2018) and Giacobbo & Mapelli (2018) have updated the recipes for stellar winds and SN explosions in BSE, producing a new version of BSE called ‘Massive Objects in Binary Stellar Evolution’ (MOBSE).

Many other population synthesis codes are based on updated versions of Hurley et al. (2000) fitting formulas, including SEBA (Portegies Zwart & Verbunt 1996; Toonen, Nelemans & Portegies Zwart 2012; Mapelli et al. 2013; Schneider et al. 2017), BINARY.C (Izzard et al. 2004, 2006, 2009), STARTRACK (Belczynski et al. 2008, 2010, 2016a) and COMPAS (Barrett et al. 2017; Stevenson, Berry & Mandel 2017).

Alternative approaches to fitting formulas consist in integrating stellar evolution on the fly (e.g. MESA, Paxton et al. 2011, 2013, 2015; BPASS, Eldridge & Stanway 2016; Eldridge et al. 2017) or in reading stellar evolution from look-up tables (e.g. SEVN Spera et al. 2015; Spera & Mapelli 2017; COMBINE, Kruckow et al. 2018). The interpolation of stellar evolution from look-up tables, containing a grid of stellar evolution models, is both convenient in terms of computing time and versatile, because the stellar evolution model can be updated by simply changing tables.

In this work, we discuss the statistics of BHBs we obtained with the SEVN code (Spera et al. 2015; Spera & Mapelli 2017). SEVN interpolates stellar evolution from look-up tables (the default tables being derived from PARSEC, Bressan et al. 2012; Chen et al. 2015), includes five different models for core-collapse SNe, contains prescriptions for PPISNe and PISNe, and has been updated to implement also binary evolution processes (wind mass transfer, Roche lobe overflow, CE, stellar mergers, tidal evolution, gravitational wave decay, and magnetic braking).

2 THE SEVN CODE

2.1 Single star evolution

2.1.1 Interpolation method

SEVN evolves the physical parameters of stars by reading a set of tabulated stellar evolutionary tracks that are interpolated on-the-fly. As default, SEVN includes a new set of look-up tables generated using the PARSEC code (Bressan et al. 2012; Chen et al. 2014; Tang et al. 2014; Chen et al. 2015). This set of tables ranges from metallicity $Z = 10^{-4}$ to $Z = 6 \times 10^{-2}$ with stars in the mass range $2 \leq M_{\text{ZAMS}} / M_{\odot} \leq 150$. Furthermore, we have used the PARSEC code to generate a new set of tracks for bare Helium cores to follow the evolution of the stars that lose the whole Hydrogen envelope after a mass-transfer phase. The look-up tables of Helium stars range from metallicity $Z = 10^{-4}$ to $Z = 5 \times 10^{-2}$ with stars in the mass range $0.4 \leq M_{\text{He-ZAMS}} / M_{\odot} \leq 150$ (see Section 2.1.2 for details).

To perform the interpolation, in SEVN we distinguish the stars that are on the main sequence (H phase) from those that have already formed an He core but not yet a Carbon–Oxygen (CO) core (He phase) and those that have already formed a CO core (CO phase). The division into three macro-phases is convenient in terms of computing time and it also ensures that the stars used for the interpolation have the same internal structure. Furthermore, we impose that the interpolating stars have the same percentage of life

Table 1. List of the integer values k used for stellar evolutionary phases and their corresponding macro-phases. A naked Helium MS is a naked Helium star burning Helium in the core. A naked Helium HG is a naked Helium star burning Helium in shells. A naked Helium giant branch is a naked Helium star burning Carbon (or a heavier element) in the core.

k	Phase	Macro-phase
0	Low-mass main sequence (MS, $M < 0.7 M_{\odot}$)	H phase
1	MS ($M > 0.7 M_{\odot}$)	H phase
2	Hertzsprung gap (HG)	He phase
3	First giant branch	He phase
4	Core He burning	He phase
5	Early asymptotic giant branch (AGB)	CO phase
6	Thermally pulsing AGB	CO phase
7	Naked Helium MS	He phase
8	Naked Helium HG	CO phase
9	Naked Helium giant branch	CO phase
10	He white dwarf (WD)	none
11	Carbon–Oxygen WD	none
12	Oxygen–Neon WD	none
13	Neutron star (NS)	none
14	black hole (BH)	none
-1	Massless remnant	none

(Θ_p) of the interpolated star on its macro-phase. For every time t , the percentage of life of a star is

$$\Theta_p = \frac{t - t_{0,p}}{t_{f,p} - t_{0,p}} \quad (1)$$

where $t_{0,p}$ is the starting time of the star's evolutionary macro-phase p (where $p = \text{H phase, He phase and CO phase}$) and $t_{f,p}$ is its final time. By using Θ_p , we ensure that the stars used for the interpolation are at the same stellar evolutionary phase within the same macro-phase.

In addition to these three macro-phases, we have defined several stellar-evolution phases. As in Hurley et al. (2002), in SEVN we use integer values to distinguish between different stellar evolution phases. Table 1 shows the list of the stellar evolutionary phases and their corresponding macro-phases used in the SEVN code. We adopt the same indexes used by Hurley et al. (2002) except for the massless remnants for which we use the index -1 instead of 15 . The stellar evolution phase of a star is evaluated using the values and the rate of change of the interpolated physical stellar parameters. It is worth noting that in SEVN we mark a star as Wolf–Rayet (WR, $k = 7, 8, 9$) if

$$\frac{|M - M_{\text{He}}|}{M} < 2 \times 10^{-2}, \quad (2)$$

where M is the total mass of the star and M_{He} is its He-core mass. The details of the interpolation method for isolated stars are discussed in the supplementary material, Appendix A1.

While for isolated stars the interpolation tracks are fixed, for binary stars we allow jumps on different tracks. Every time a star has accreted (donated) a significant amount of mass Δm from (to) its companion, the SEVN code moves on to another evolutionary track in the look-up tables. The value of Δm depends on the binary evolution processes (see Section 2.3) but we allow jumps to new tracks only if

$$\Delta m > \gamma_m M, \quad (3)$$

where M is the total mass of the star and γ_m is a parameter with typical value of ~ 0.01 . The jumps on to new tracks depend primarily on the star's macro-phase. For a star in the H phase, we search for

new interpolating stars with (i) $t < t_{f,\text{H phase}}$, (ii) the same percentage of life of the star, and (iii) the same total mass.

For a star in the He phase, the interpolating stars must have $t > t_{0,\text{He phase}}$ and the same He core mass. If the interpolated star is not a WR star, we also impose that the new track has the same mass of the H envelope.

For stars in the CO phase, we use the same strategy adopted for stars in the He phase but we require that $t > t_{0,\text{CO phase}}$. In all cases, if the requirements are not matched, we use the best interpolating stars the algorithm was able to find. The details of the track-finding method are discussed in the supplementary material, Appendix A2.

2.1.2 Helium stars

The evolution of the He stars is computed starting from a Helium ZAMS (He-ZAMS) obtained by removing the H-rich envelope of a normal star at the beginning of the central He-burning phase and, thereafter, varying its total mass keeping the chemistry fixed.

The initial mass on the He-ZAMS varies from $0.36 M_{\odot}$ to $150 M_{\odot}$ with increasing mass steps of $0.02, 0.05, 0.10, 0.20, 0.50, 1.0, 2.0, 5.0, 20.0 M_{\odot}$ respectively above $0.36, 0.5, 0.8, 2, 9, 12, 20, 40, 100 M_{\odot}$.

The basic input physics is the same as that described in Bressan et al. (2012) and Chen et al. (2015), apart from the following small changes. The nuclear reaction rates from the JINA REACLIB database (Cyburt et al. 2010) have been updated to their recommended values of April 6, 2015 (Fu et al. 2018). The equation of state for He and CO-rich mixtures has been extended to slightly lower temperatures, as well as the corresponding radiative opacities. We account for mass loss adopting the same mass-loss rates used for the PARSEC evolutionary tracks of massive stars in the WR phases (Chen et al. 2015).

The evolution of selected sets of naked He-star models is shown in Fig. 1 and Fig. 2 for $Z = 2 \times 10^{-4}$ and $Z = 2 \times 10^{-2}$, respectively. Here, we briefly describe the evolution of the He stars with solar metallicity leaving a more thorough discussion to a companion paper.

The evolution on the Helium main sequence (He-MS) is very similar for all masses and characterized by a growing temperature as the central He is burned. At central He exhaustion, the evolution is reversed and the stars move towards the asymptotic giant branch (AGB) or red super-giant branch (RSGB), at least for initial masses below about $15 M_{\odot}$. For the stars with the lower masses ($0.36 M_{\odot} - 0.9 M_{\odot}$), the mass-loss is high enough to remove the surrounding He-rich envelope before they reach the AGB and they evolve along the so called *AGB-manqué* phase and cool down along the CO-rich white dwarf (WD) sequence (see the tracks of the models with $M_{\text{He-ZAMS}} = 0.5, 0.6, \text{ and } 0.8 M_{\odot}$).

As in the case of the low-mass H-rich stars, the post-AGB phase is faster at increasing mass.

He stars with mass between $1.0 M_{\odot} - 2.4 M_{\odot}$ evolve towards the AGB branch and the equation of state in their central regions begins to be dominated by degenerate electrons. Stars with initial mass below $1.4 M_{\odot}$ end their lives as CO WDs because mass loss is able to decrease their current mass below the threshold for Carbon ignition. He stars with initial mass between $1.4 M_{\odot}$ and $2.4 M_{\odot}$ could still ignite Carbon while not having a strongly degenerate electron core. To better understand the evolution of these stars, we have followed in more detail the evolution of He stars with initial mass between $1.5 M_{\odot}$ and $2.4 M_{\odot}$. For $Z = 0.0002$, we find that stars with $M_{\text{He-ZAMS}}$ between $1.8 M_{\odot}$ and $2.2 M_{\odot}$ are able to

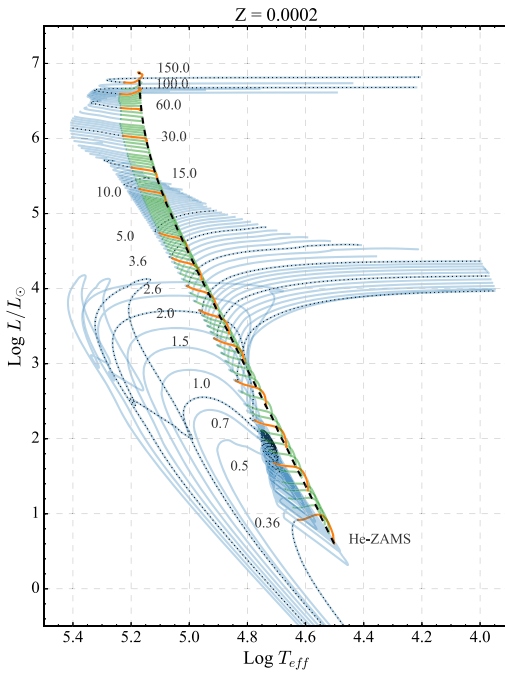


Figure 1. Hertzsprung–Russell (HR) diagram of the pure He–star tracks, at $Z = 2 \times 10^{-4}$. The He-ZAMS is indicated by the black dashed line. The central He-Burning phase is plotted in green (in orange for the labelled masses) to better show the width of the most populated area in the HR diagram. The remaining evolution (post He-MS) is coloured in blue.

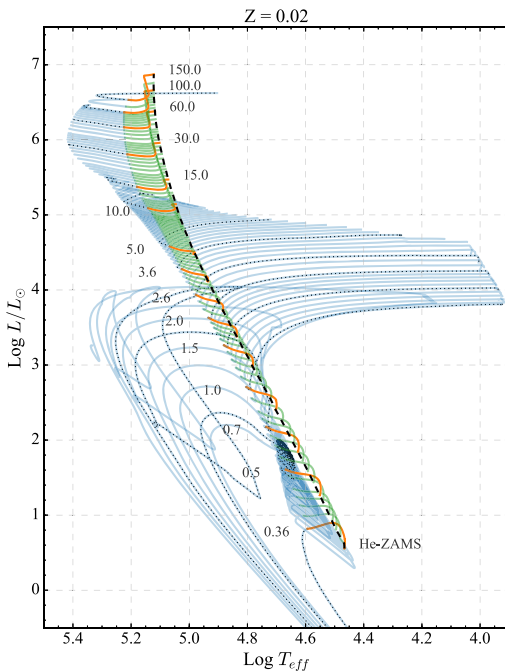


Figure 2. Same as Fig. 2 but for $Z = 2 \times 10^{-2}$.

ignite Carbon and, through a series of off centre Carbon burning episodes, they build up a degenerate Oxygen–Neon–Magnesium core. These stars become super AGB stars and their following fate is then dictated by the competition between the core growth by the

Helium/Carbon burning shells and the envelope consumption by mass loss.

If the mass-loss process is high enough to prevent the core mass to reach the threshold density for the onset of electron capture processes on ^{24}Mg and ^{20}Ne nuclei, then the star will become an Oxygen–Neon–Magnesium WD. Alternatively, the star will end its life as an electron-capture SN. The threshold core mass is confined between $M_{\text{CO}} \simeq 1.38 M_{\odot}$ (Miyaji et al. 1980) and $M_{\text{CO}} \simeq 1.37 M_{\odot}$ (Nomoto 1984; Takahashi, Yoshida & Umeda 2013). The model with He-ZAMS mass $M_{\text{He-ZAMS}} = 1.8 M_{\odot}$ is evolved until its total mass is $M = 1.3 M_{\odot}$ and the core mass is $M_{\text{CO}} \sim 1.095 M_{\odot}$. For the track with $M_{\text{He-ZAMS}} = 1.9 M_{\odot}$, the last computed model has a total mass of $M = 1.2 M_{\odot}$ and a core mass of $M_{\text{CO}} \sim 1.179 M_{\odot}$, while for the $M_{\text{He-ZAMS}} = 2.0 M_{\odot}$ track, the last computed model has a total mass of $M = 1.2 M_{\odot}$ and a core mass of $M_{\text{CO}} \sim 1.218 M_{\odot}$. These three models will become O–Ne–Mg WDs.

The model with $M_{\text{He-ZAMS}} = 2.2 M_{\odot}$ is followed until the current mass and the core mass are $M = 1.454 M_{\odot}$ and $M_{\text{CO}} = 1.301 M_{\odot}$, respectively. The central density at this stage is $\rho_c = 4.40 \times 10^8 \text{ g cm}^{-3}$, while the central and the off centre temperatures are $T_c = 2.39 \times 10^8 \text{ K}$ and $T_{\text{max}} = 6.34 \times 10^8 \text{ K}$, respectively. This star has almost reached the mass threshold for the ignition of Neon in an electron degenerate gas, but we cannot follow this phase because our network does not yet include electron-capture reactions. A simple extrapolation indicates that with the current mass-loss and core-growth rates, a $\sim 0.084 M_{\odot}$ envelope can be lost before the core reaches the critical mass for Neon ignition (~ 0.0004 Myr is the time required for the former against ~ 0.0179 Myr for the latter). Thus, this mass could be the separation mass between O–Ne–Mg WDs and electron capture SNe.

The model with $M_{\text{He-ZAMS}} = 2.4 M_{\odot}$ is followed until the central density reaches $\rho_c = 2.41 \times 10^8 \text{ g cm}^{-3}$ and the central temperature is $T_c = 5.39 \times 10^8 \text{ K}$. At this point, the core mass is $M_{\text{CO}} \sim 1.39 M_{\odot}$. The star has a total mass of $M = 2.28 M_{\odot}$ and an off centre maximum temperature of $T_{\text{max}} = 1.87 \times 10^9 \text{ K}$. In the off centre region near the maximum temperature, Neon has been almost completely burned and, given the high central density and degeneracy, it is likely that the core will soon begin the electron capture collapse. Similar properties are found for models with $Z = 0.02$. The track with mass $M_{\text{He-ZAMS}} = 2.4 M_{\odot}$ is followed until the central density reaches $\rho_c = 1.860 \times 10^8 \text{ g cm}^{-3}$, with a central temperature of $T_c = 3.645 \times 10^8 \text{ K}$ and an off centre maximum temperature of $T_{\text{max}} = 9.420 \times 10^8 \text{ K}$. At this stage, the core mass is $M_{\text{CO}} \sim 1.301 M_{\odot}$ and the total mass is $M_{\text{cur}} \sim 1.865 M_{\odot}$. An extrapolation adopting the current mass-loss rate and He-core growth rate indicates that the model will reach the critical core mass for Neon ignition about 10 times faster than what is required by mass loss to peel off the envelope to below the same limit. In contrast, the opposite occurs for the model of initial \times mass $M_{\text{He-ZAMS}} = 2.2 M_{\odot}$.

More massive stars are evolved until the beginning of Oxygen burning.

2.1.3 Stellar spin

We follow the evolution of stellar spin Ω_{spin} by taking into account the change of moment of inertia, mass loss by stellar winds, magnetic braking, and mass transfer. We compute the moment of inertia as in Hurley et al. (2000):

$$I = 0.1 M_c R_c^2 + 0.21 (M - M_c) R^2, \quad (4)$$

where M and R are the stellar mass and radius, while M_c and R_c are the core mass and radius.

We assume that stellar winds carry away spin angular momentum uniformly from a thin shell at the stellar surface. We include spin-down by magnetic braking for giant stars with convective envelopes (type $k = 2\text{--}6$, see eq. (111) of Hurley et al. 2000).

In this work, we neglect the effect of stellar spin on wind mass loss. The enhancement of stellar winds due to rotation will be investigated in a forthcoming work.

We evolve stellar spins even if the PARSEC stellar tracks we use in this paper are calculated for non-rotating stars. Although not fully consistent, this approach has been followed in the past by most population synthesis codes, to enable the calculation of tidal forces and other spin-dependent binary evolution processes. In future works, we will include rotating stellar evolutionary tracks from Costa et al. (in preparation).

2.2 Prescriptions for supernovae (SNe)

The prescriptions for SNe adopted in SEVN were already described in Spera et al. (2015) and in Spera & Mapelli (2017). Here, below, we briefly summarize the most important features, while we refer the reader to the supplementary material, Appendix B, for more details. SEVN contains five different models for core-collapse SNe, which can be activated with a different option in the parameter file. These are (i) the rapid core-collapse model (Fryer et al. 2012), (ii) the delayed core-collapse model (Fryer et al. 2012), (iii) the prescription implemented in the STARTRACK code (Belczynski et al. 2010), (iv) a model based on the compactness parameter (O'Connor & Ott 2011), and the (v) two-parameter criterion by Ertl et al. (2016). In this work, we adopt the rapid core-collapse SN model as the reference model.

PISNe and PPISNe are also included in SEVN following the prescriptions discussed in Spera & Mapelli (2017).

Finally, the SN kicks are implemented in SEVN adopting the Hobbs et al. (2005) kick distribution for both neutron stars (NSs) and BHs but we scale the kick by the amount of fallback (Fryer et al. 2012):

$$V_{\text{kick}} = (1 - f_{\text{fb}}) W_{\text{kick}}, \quad (5)$$

where f_{fb} is the fallback factor (the explicit expression can be found in Giacobbo et al. 2018), and W_{kick} is randomly drawn from the Maxwellian distribution derived by Hobbs et al. (2005). According to this formalism, if a BH forms by prompt collapse of the parent star $V_{\text{kick}} = 0$.

If the SN occurs when the BH or NS progenitor is member of a binary, the SN kick can unbind the system. The survival of the binary system depends on the orbital elements at the moment of the explosion and on the SN kick. If the binary remains bound, its post-SN semimajor axis and eccentricity are calculated as described in the appendix A1 of Hurley et al. (2002).

2.3 Binary evolution

2.3.1 Mass transfer

Mass transfer has been implemented in SEVN following the prescriptions described in Hurley et al. (2002) with few important updates. SEVN considers both wind mass transfer and Roche lobe overflow. Here, below we give a summary of our implementation, highlighting the differences with respect to BSE (Hurley et al. 2002). This

while we refer to the supplementary material, Appendix C, for more details.

The mean accretion rate by stellar winds is calculated from the Bondi & Hoyle (1944) formula, following Hurley et al. (2002). Mass transfer by stellar winds is definitely a non-conservative mass transfer process. Thus, we describe also the change of orbital angular momentum, stellar spin, and eccentricity following Hurley et al. (2002).

At every time-step, we evaluate whether one of the two members of the binary fills its Roche lobe by calculating the Roche lobe as (Eggleton 1983)

$$R_{L,i} = a \frac{0.49 q_i^{2/3}}{0.6 q_i^{2/3} + \ln(1 + q_i^{1/3})}, \quad (6)$$

where $q_i = M_i/M_j$ with $i = 1, j = 2$ ($i = 2, j = 1$) for the primary (secondary) star. If $R_1 \geq R_{L,1}$, mass is transferred from the primary to the secondary. We allow for non-conservative mass transfer, which means that the mass lost by the primary at every time-step Δm_1 can be larger than the mass accreted by the secondary Δm_2 .

If the Roche lobe filling donor is a neutron star (NS, $k = 13$) or a BH ($k = 14$), the accretor must be another NS or BH. In this case, the two objects are always merged.

In all the other cases, to decide the amount of mass transferred from the primary Δm_1 , we first evaluate the stability of mass transfer using the radius–mass exponents ζ defined by Webbink (1985). If the mass transfer is found to be unstable over a dynamical time-scale, the stars are merged (if the donor is a main sequence or an Hertzsprung–gap star) or enter CE (if the donor is in any other evolutionary phase).

If the mass transfer is stable, the mass loss rate of the primary is described as

$$\dot{M}_1 = 3 \times 10^{-6} M_{\odot} \text{ yr}^{-1} \left(\frac{M_1}{M_{\odot}} \right)^2 \left[\ln(R_1/R_{L,1}) \right]^3. \quad (7)$$

This is similar to equation (58) of Hurley et al. (2002), but with an important difference: unlike Hurley et al. (2002), we do not need to put any threshold to the dependence on M_1^2 to obtain results that are consistent with BSE. The term $[\ln(R_1/R_1)]^3$ accounts for the fact that mass loss should increase if the Roche lobe is overfilled. If the primary is a degenerate star, \dot{M}_1 is increased by a factor $10^3 M_1 / \max(R_1/R_{\odot}, 10^{-4})$.

Finally, if mass transfer is dynamically stable but unstable over a thermal time-scale, the mass lost by the primary is calculated as the minimum between the result of equation (7) and the following equation:

$$\dot{M}_1 = \begin{cases} \frac{M_1}{\tau_{K1}} & \text{if } k = 2, 3, 4, 5, 6, 8, 9 \\ \frac{M_1}{\tau_{D1}} & \text{if } k = 0, 1, 7 \end{cases} \quad (8)$$

where τ_{K1} is the Kelvin–Helmholtz time-scale and τ_{D1} is the dynamical time-scale of the donor. These time-scales are defined as in Hurley et al. (2002).

In the case of a stable or thermally unstable mass transfer, if the accretor is a non-degenerate star, we assume that the accretion is limited by the thermal time-scale of the accretor, as described by Hurley et al. (2002). In particular, the accreted mass Δm_2 is

$$\Delta m_2 = \min \left(\alpha_{\tau} \frac{M_2}{\dot{M}_1 \tau_{K2}}, 1 \right) \Delta m_1, \quad (9)$$

where Δm_1 is the mass lost by the donor, τ_{K2} is the Kelvin–Helmholtz time-scale of the accretor, and α_{τ} is a dimensionless efficiency parameter ($\alpha_{\tau} = 10$ according to Hurley et al. 2002). This

is a crucial difference with respect to other population synthesis codes (e.g. STARTRACK, Belczynski et al. 2008), which assume that the accreted mass is $\Delta m_2 = f_a \Delta m_1$, where $0 \leq f_a \leq 1$ is a constant efficiency factor, without accounting for the response of the secondary.

With respect to Hurley et al. (2002), we introduce an important difference in the treatment of a Wolf–Rayet (WR, $k = 7, 8, 9$) accretor in a stable or a thermally unstable Roche lobe phase: we assume that if the donor has a Hydrogen envelope ($k = 0, 1, 2, 3, 4, 5, 6$), the WR does not accrete any Hydrogen. In contrast, Hurley et al. (2002) assume that the WR accretes a Hydrogen envelope, becoming a core Helium burning (cHeB) or an AGB star. We make this choice because the winds of the WR are expected to eject a tiny envelope very fast with respect to our time-steps.

If the accretor is a degenerate star, WD ($k = 10, 11, 12$), NS ($k = 13$) or BH ($k = 14$), the accreted mass is estimated as:

$$\Delta m_2 = \min(\Delta m_1, \Delta m_e), \quad (10)$$

where

$$\Delta m_e = 2.08 \times 10^{-3} M_\odot f_{\text{Edd}} (1.0 + X)^{-1} \left(\frac{R_2}{R_\odot} \right) \left(\frac{dt}{\text{yr}} \right). \quad (11)$$

In equation (11), X is the Hydrogen fraction of the donor star, R_2 is the radius of the accretor (for a BH, we use the Schwarzschild radius), dt is the time-step in yr, and f_{Edd} is a dimensionless factor indicating whether we allow for super-Eddington accretion (in this paper, we assume $f_{\text{Edd}} = 1$, which corresponds to Eddington-limited accretion).

If the accretor is a WD, we also consider the possibility of nova eruptions, following the treatment of Hurley et al. (2002).

If the mass change (of the donor or the accretor) induced by mass transfer is $\Delta m > \gamma_m M$ (see equation (3)), then SEVN finds a new track as described in Section 2.1.1.

Finally, the variation of orbital angular momentum and stellar spins induced by non-conservative Roche lobe overflow mass transfer is implemented as in Hurley et al. (2002) and summarized in the supplementary material, Appendix C.

2.3.2 Common envelope and stellar mergers

In SEVN, a common envelope (CE) evolution is the result of (i) a Roche lobe overflow unstable on a dynamical time-scale, or (ii) a collision at periaxis between two stars,² or (iii) a contact binary, i.e. a binary where both stars fill their Roche lobes ($R_1 \geq R_{\text{L},1}$ and $R_2 \geq R_{\text{L},2}$ at the same time).

In these three aforementioned cases, if the donor is a main sequence (MS) or a Hertzsprung-gap (HG) star, the two stars are merged directly, without even calculating the CE evolution. In this case, we assume that the binary will not survive CE evolution, because the donor lacks a well-developed core (Dominik et al. 2012). In contrast, if the donor star has a well-developed core ($k = 3, 4, 5, 6, 8, 9$), the binary enters the routine calculating the CE phase.

During a CE phase, the core of the donor and the accretor are engulfed by the donor's envelope. They begin to spiral in transferring energy to the CE. If the energy released is sufficient to eject the entire envelope, the system survives; otherwise, the donor coalesces with the accretor. To derive the outcomes of the CE

²A collision happens at periaxis when $(R_1 + R_2) > (1 - e)a$.

evolution, we follow the same formalism as described by Hurley et al. (2002).

This formalism is based on two parameters (Webbink 1984; de Kool 1992; Ivanova et al. 2013): α is the fraction of the orbital energy released during the spiral-in phase and converted into kinetic energy of the envelope, and λ is a structural parameter used to define the binding energy of the envelope.

We can write the initial binding energy of the CE as

$$E_{\text{bind},i} = -\frac{G}{\lambda} \left(\frac{M_1 M_{1,\text{env}}}{R_1} + \frac{M_2 M_{2,\text{env}}}{R_2} \right), \quad (12)$$

where $M_{1,\text{env}}$ and $M_{2,\text{env}}$ are the initial masses of the envelope of the primary and of the secondary, respectively.

The fraction of orbital energy which goes into kinetic energy of the envelope is

$$\Delta E_{\text{orb}} = -\alpha (E_{\text{orb},f} - E_{\text{orb},i}) = \alpha \frac{G M_{\text{c},1} M_{\text{c},2}}{2} \left(\frac{1}{a_f} - \frac{1}{a_i} \right), \quad (13)$$

where $E_{\text{orb},f}$ ($E_{\text{orb},i}$) is the orbital energy of the binary after (before) the CE phase, a_f (a_i) is the semimajor axis after (before) the CE phase, $M_{\text{c},1}$ and $M_{\text{c},2}$ are the masses of the cores of the two stars. If the secondary is a degenerate remnant or a naked core, then $M_{\text{c},2}$ is the total mass of the star.

By imposing that $E_{\text{bind},i} = \Delta E_{\text{orb}}$, we can derive the final semimajor axis a_f for which the CE is completely ejected. The binary survives and the entire envelope is ejected if neither core fills its post-CE Roche lobe, estimated from equation (6) assuming $a = a_f$, $q_1 = M_{\text{c},1}/M_{\text{c},2}$ and $q_2 = M_{\text{c},2}/M_{\text{c},1}$. The resulting post-CE binary has masses $M_1 = M_{\text{c},1}$, $M_2 = M_{\text{c},2}$ and semimajor axis a_f . Then, SEVN finds a new track for each naked core (unless the accretor is a compact remnant).

In contrast, the two stars are merged if either of their cores fills its post-CE Roche lobe. We estimate the binding energy of the envelope which remains bound to the system as

$$E_{\text{bind},f} = E_{\text{bind},i} + \alpha \left(\frac{G M_{\text{c},1} M_{\text{c},2}}{2 a_L} + E_{\text{orb},i} \right), \quad (14)$$

where a_L is the semimajor axis for which the larger core fills its post-CE Roche lobe.

The merger product will have core mass $M_{\text{c},3} = M_{\text{c},1} + M_{\text{c},2}$, total mass M_3 , and radius R_3 . To estimate the value of M_3 and R_3 , SEVN finds a new track with envelope binding energy equal to $E_{\text{bind},f}$ and with core mass $M_{\text{c},3}$, assuming that the envelope binding energy of the merger product is

$$E_{\text{bind},f} = -\frac{G M_3 (M_3 - M_{\text{c},3})}{\lambda R_3}. \quad (15)$$

The spectral type and the other properties of the merger product are thus uniquely determined by the track found by SEVN through this search. This procedure is significantly different with respect to the one implemented by Hurley et al. (2002). In BSE, the final mass M_3 is found by assuming a relation between mass and radius ($R \propto M^{-x}$) and then by solving the relation between M_3 and the other relevant quantities ($M_{\text{c},3}$, M_1 , M_2 , $E_{\text{bind},i}$ and $E_{\text{bind},f}$) numerically. With SEVN, the values of M_3 and R_3 are determined self-consistently by the search algorithm.

Another substantial upgrade with respect to BSE is that SEVN does not need to use a 'matrix of stellar types' as the one reported in table 2 of Hurley et al. (2002). In fact, to determine the stellar type of the merger product, BSE reads a matrix where the type of the merger product is given by the combination of the stellar types of the two merged stars. In contrast, SEVN does not need any

'artificially' defined spectral type, because the spectral type is the natural result of the search algorithm described above. This holds both for colliding unevolved stars (MS and HG stars) and post-CE mergers.

The only exception to the formalism described above is the case in which a star merges with a BH (or an NS) after a CE phase. In the latter case, we assume that the final object remains a BH (or an NS) and that none of the mass of the donor star is accreted by the BH (or NS).

2.3.3 Tidal evolution

We implement the tidal equilibrium model of Hut (1981), which is based on the weak friction approximation and constant time lag model. In this model, the misalignment of the tidal bulges with respect to the perturbing potential allows spin-orbit coupling and dissipation of orbital energy. We evolve semimajor axis, eccentricity, and spin using the secular-averaged equations of Hut (1981):

$$\frac{1}{a} \frac{da}{dt} = -6 \left(\frac{k}{T} \right) q(q+1) \left(\frac{R}{a} \right)^8 \frac{1}{(1-e^2)^{15/2}} \cdot \left\{ f_1(e^2) - (1-e^2)^{2/3} f_2(e^2) \frac{\Omega_{\text{spin}}}{\Omega_{\text{orb}}} \right\} \quad (16)$$

$$\frac{1}{e} \frac{de}{dt} = -27 \left(\frac{k}{T} \right) q(q+1) \left(\frac{R}{a} \right)^8 \frac{1}{(1-e^2)^{13/2}} \cdot \left\{ f_3(e^2) - \frac{11}{18} (1-e^2)^{2/3} f_4(e^2) \frac{\Omega_{\text{spin}}}{\Omega_{\text{orb}}} \right\} \quad (17)$$

$$\frac{d\Omega_{\text{spin}}}{dt} = 3 \left(\frac{k}{T} \right) \frac{q^2}{r_g^2} \left(\frac{R}{a} \right)^6 \frac{\Omega_{\text{orb}}}{(1-e^2)^6} \cdot \left\{ f_2(e^2) - (1-e^2)^{2/3} f_5(e^2) \frac{\Omega_{\text{spin}}}{\Omega_{\text{orb}}} \right\} \quad (18)$$

where q is the mass ratio between the perturbing star and the star undergoing tides, while $r_g^2 = I/M R^2$, Ω_{spin} , and R are the gyration radius, spin, and radius of the star undergoing tides, respectively. The $f_i(e^2)$ terms are polynomial functions of the eccentricity given by Hut (1981). In this work, we assume that the stars have zero obliquity, i.e. the spin is aligned with the angular momentum vector of the binary.

The term k/T determines the time-scale of the tidal evolution and depends on the dissipation mechanism responsible for the misalignment of the tidal bulges. We adopt the prescriptions of Hurley et al. (2002), which are based on Zahn (1975) for the tide in radiative envelopes and Zahn (1977) for the tide in convective envelopes (see also Rasio et al. 1996).

2.3.4 Gravitational-wave decay

Gravitational wave (GW) decay is implemented in SEVN according to the formulas by Peters (1964), which describe the loss of energy and angular momentum of a system due to the radiation of GWs. In particular, the loss of orbital angular momentum and the loss of eccentricity due to GW emission are estimated as

$$\frac{J_{\text{orb}}}{J_{\text{orb}}} = -\frac{32}{5} \frac{G^3}{c^5} \frac{M_1 M_2 (M_1 + M_2)}{a^4} \frac{1 + \frac{7}{8} e^2}{(1-e^2)^{5/2}} \quad (19)$$

$$\frac{\dot{e}}{e} = -\frac{32}{5} \frac{G^3}{c^5} \frac{M_1 M_2 (M_1 + M_2)}{a^4} \frac{\frac{19}{9} + \frac{121}{96} e^2}{(1-e^2)^{5/2}} \quad (20)$$

Equations (19) and (20) are evaluated for all double compact-object binaries ($k \geq 10$) and not only for the closest ones (in contrast, BSE calculates the GW decay only if $a \leq 10R_{\odot}$).

2.4 Comparison of SEVN with BSE and MOBSE

Fig. 3 shows the time evolution of the total star mass (M), the stellar radius R , the He core mass M_{He} , and the He radius R_{He} for three selected massive stars ($M_{\text{ZAMS}} = 30, 80$, and $120 M_{\odot}$), at different metallicity Z . The results obtained with the SEVN code (solid lines) are compared to those obtained with BSE (dotted lines) and MOBSE (dashed lines). The star with $M_{\text{ZAMS}} = 120 M_{\odot}$ is not evolved with the BSE code because the fitting formulas implemented in BSE may be inaccurate for $M_{\text{ZAMS}} > 100 M_{\odot}$ (Hurley et al. 2002).

From Fig. 3, it is apparent that the star lifetime in SEVN is up to ~ 30 per cent shorter than that obtained with MOBSE and BSE. SEVN and MOBSE show a similar evolution of M for all considered metallicities Z and for all selected M_{ZAMS} (Fig. 3, panels *a1*, *a2*, and *a3*). In contrast, BSE predicts a different evolution for the $80 M_{\odot}$ star, especially in the late evolutionary stages for $Z \lesssim 6 \times 10^{-3}$, because of different stellar wind models. The difference is maximum at $Z = 10^{-4}$ (panel *a3*), where BSE predicts the formation of a WR star with $M \simeq 12 M_{\odot}$ while SEVN forms a red hypergiant star with $M \simeq 80 M_{\odot}$.

The evolution of R shows even more differences. According to SEVN, at $Z = 2 \times 10^{-2}$ (panel *b1*), the stars with $M_{\text{ZAMS}} = 80$ and $120 M_{\odot}$ become WR stars before reaching the red giant branch, therefore their radius is always $< 80 R_{\odot}$. In contrast, in MOBSE, they become WR stars at a later stage, after having already gone through the red giant branch and having reached $R > 2 \times 10^3 R_{\odot}$.

Furthermore, for the $30 M_{\odot}$ star, both BSE and MOBSE predict the formation of a WR star ($R = R_{\text{He}} \simeq 1 R_{\odot}$) while, in SEVN, the star ends its life as a red supergiant ($R \simeq 10^3 R_{\odot}$) with a Hydrogen-envelope mass of $\sim 5 M_{\odot}$.

According to SEVN, at $Z = 6 \times 10^{-3}$ (panel *b2*), both the $80 M_{\odot}$ and the $120 M_{\odot}$ star die as WR stars, with $R \lesssim 2 R_{\odot}$. In contrast, according to MOBSE, the same stars die as red supergiants with $R \gtrsim 3 \times 10^3 R_{\odot}$.

The evolution of R is quite similar at $Z = 10^{-4}$ (panel *b3*), even though SEVN forms stars with smaller radii compared to those formed with MOBSE ($\sim 1.5 \times 10^3 R_{\odot}$ against $\gtrsim 4 \times 10^3 R_{\odot}$).

The three codes show a quite similar evolution of M_{He} (panels *c1*, *c2*, and *c3*), with SEVN forming slightly more massive He cores (up to 15 per cent) at $Z = 10^{-4}$.

Furthermore, SEVN forms He-core radii up to 70 per cent smaller than those obtained with MOBSE and BSE, except for the $80 M_{\odot}$ and the $120 M_{\odot}$ stars at $Z = 2 \times 10^{-2}$ (panels *d1*, *d2*, and *d3*).

2.5 Initial conditions

We have run 15 sets of simulations with metallicity $Z = 4 \times 10^{-2}$, 3×10^{-2} , 2×10^{-2} , 1.6×10^{-2} , 10^{-2} , 8×10^{-3} , 6×10^{-3} , 4×10^{-3} , 2×10^{-3} , 1.6×10^{-3} , 10^{-3} , 8×10^{-4} , 4×10^{-4} , 2×10^{-4} , 10^{-4} , respectively. Each simulation set consists of 10^7 binary systems. We used the same set of initial conditions for all simulations. The masses of the primary stars (M_1) are drawn from a Kroupa initial mass function (IMF, Kroupa 2001)

$$\xi(M_1) \propto M_1^{-2.3} \quad M_1 \in [10, 150] M_{\odot}. \quad (21)$$

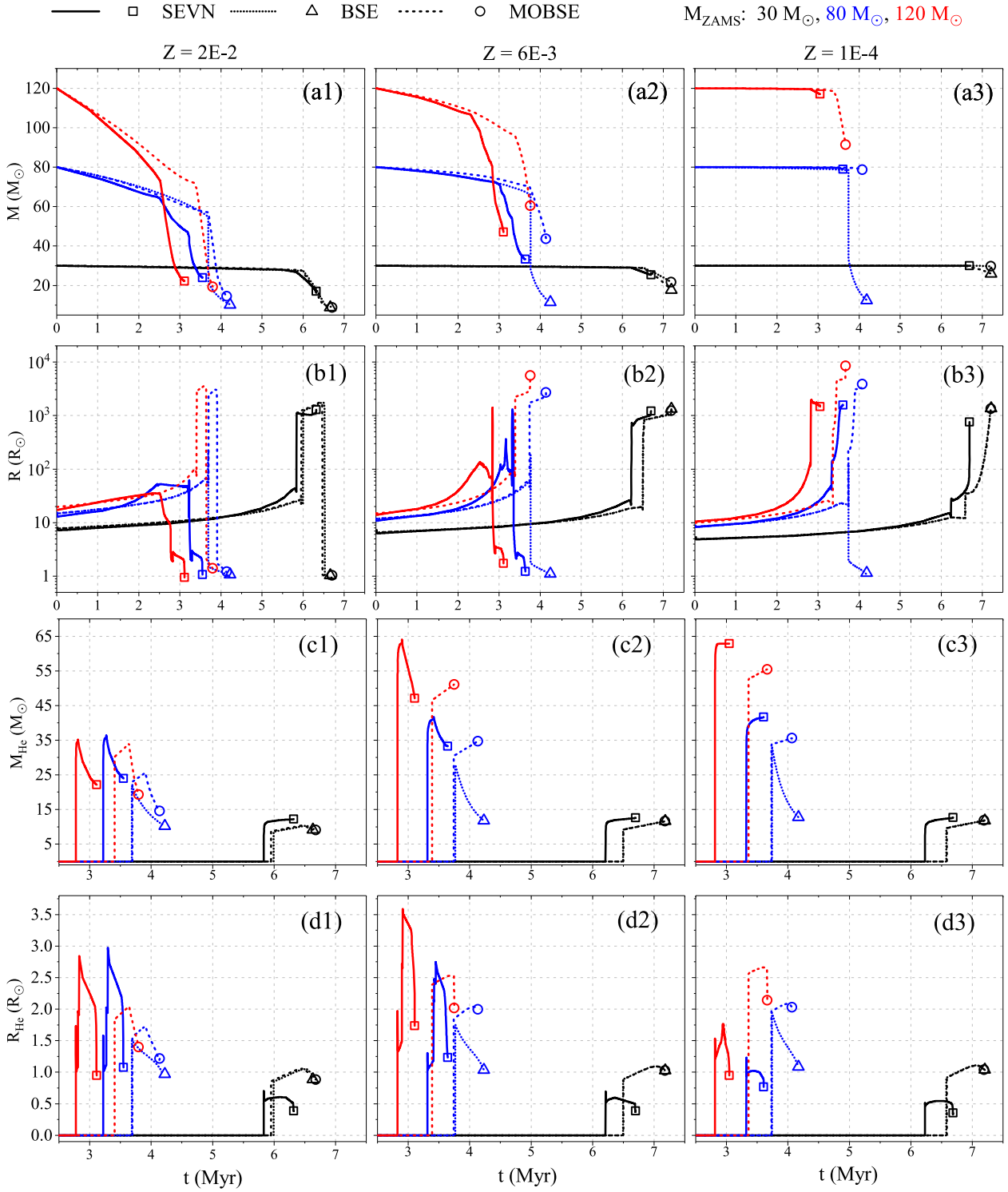


Figure 3. Time evolution of the physical stellar parameters of different stars, derived with BSE, MOBSE, and SEVN. The black, blue, and red lines refer to a star with $M_{\text{ZAMS}} = 30 M_{\odot}$, $80 M_{\odot}$ and $120 M_{\odot}$, respectively. Top row (i.e. panels labelled with *a*): total stellar mass; second row (*b*): stellar radius; third row (*c*): He-core mass; bottom row (*d*): He-core radius. Left-hand column (i.e. panels labelled with *l*): metallicity $Z = 0.02$; central column (2): $Z = 6 \times 10^{-3}$; right-hand column (3): $Z = 10^{-4}$. Solid lines: SEVN; dotted lines: BSE; dashed lines: MOBSE. The open squares identify the final point of the curves obtained with SEVN (open triangles: BSE; open circles: MOBSE). We do not evolve the star with $M_{\text{ZAMS}} = 120 M_{\odot}$ with BSE, because the fitting formulas included in BSE might be inaccurate for $M_{\text{ZAMS}} > 100 M_{\odot}$.

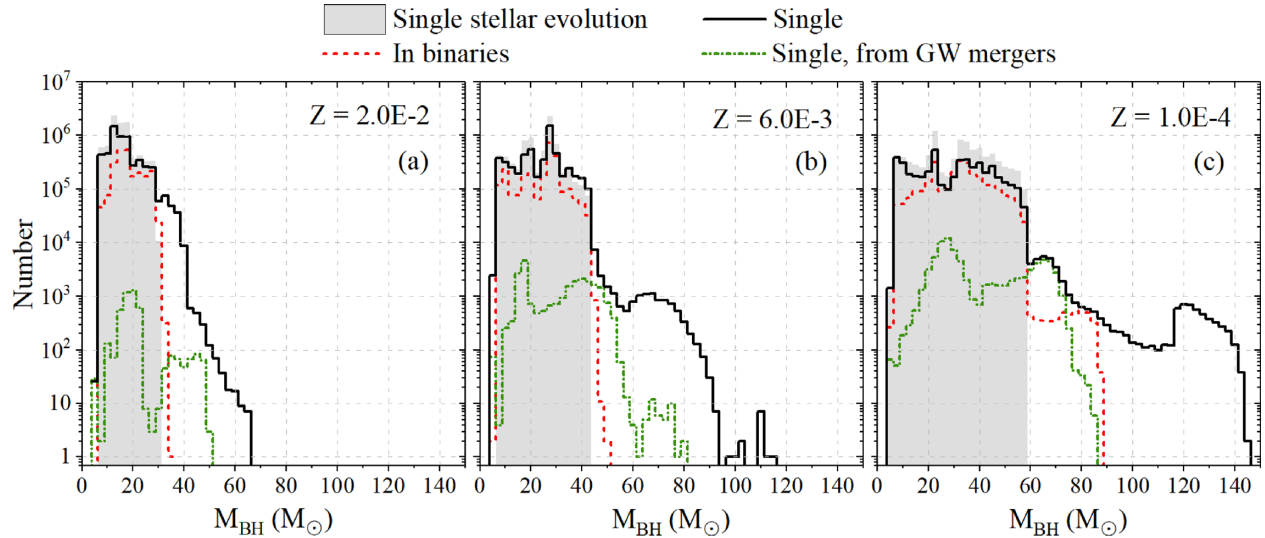


Figure 4. Distribution of the masses of BHs formed in our simulations. Dashed red line: BHs in compact-object binaries; solid black line: single BHs; dash-dotted green line: single BHs that formed from a GW merger. Grey area: BH mass distribution from single star evolution. Left-hand panel (a): $Z = 2 \times 10^{-2}$; central panel (b): $Z = 6 \times 10^{-3}$; right-hand panel (c): $Z = 10^{-4}$.

We chose $10 M_{\odot}$ as the lower mass limit of the IMF because in this work we focus only on the formation and evolution of BH binaries. We will extend the IMF range in forthcoming works.

The masses of the secondary stars (M_2) are distributed according to Sana et al. (2012)

$$\xi(q) \propto q^{-0.1} \quad q = \frac{M_2}{M_1} \in [0.1, 1] \quad \text{and} \quad M_2 \geq 10 M_{\odot}. \quad (22)$$

The initial orbital periods (\mathcal{P}) and eccentricities (e) also follow the distributions given by Sana et al. (2012),

$$\xi(\mathcal{P}) \propto \mathcal{P}^{-0.55} \quad \mathcal{P} = \log(P/\text{day}) \in [0.15, 5.5], \quad (23)$$

$$\xi(e) \propto e^{-0.42} \quad e \in [0, 1]. \quad (24)$$

We evolve each binary system for 20 Myr to ensure that both stars have ended their evolution by the end of the simulation. Furthermore, we adopt the *rapid* model for all the SN explosions and $(\alpha, \lambda) = (1, 0.1)$ for the common envelope phase.

3 RESULTS

Fig. 4 shows the distribution of BH masses in our simulations, at different metallicity. We show the masses of single BHs (solid black line), single BHs that form from GW mergers (dash-dotted green line) and BHs which are members of compact-object binaries (dashed red lines). We stress that all BHs at the end of our simulations are either single or members of compact-object binaries, because all stars have turned to compact objects by the end of the simulations.

Fig. 4 also shows that the mass distribution of BHs in compact-object binaries is not significantly different from the one we obtain from single stellar evolution (grey area in Fig. 4).

In contrast, the distribution of masses of single BHs is very different, especially at low Z . At $Z = 6 \times 10^{-3}$ ($Z = 10^{-4}$), we form single BHs with mass up to $\sim 90 M_{\odot}$ ($145 M_{\odot}$), while the maximum mass of BHs in compact-object binaries is $\sim 40 M_{\odot}$ ($\sim 90 M_{\odot}$). Most massive single BHs come from the merger of an

evolved star with an MS star, and only a small fraction of them come from GW mergers (see Section 4 for a detailed discussion).

Fig. 5 shows the mass spectrum of compact remnants which are members of double compact-object binaries. The first column (a) shows all compact objects, while the second (b) and the third column (c) show only the compact objects which form from the primary and the secondary star,³ respectively.

At $Z = 2 \times 10^{-2}$, the BHs in compact-object binaries have masses in the range $[5, 30] M_{\odot}$, with the heaviest BHs formed from stars with $M_{\text{ZAMS}} \simeq 115 M_{\odot}$. BHs can be more massive at low metallicity because their progenitor stars lose less mass through stellar winds during their life. The most massive BHs at $Z = 6 \times 10^{-3}$ have mass $\sim 45 M_{\odot}$ and they form from stars with $M_{\text{ZAMS}} \simeq 145 M_{\odot}$.

At $Z = 10^{-4}$, the heaviest BHs ($\sim 55 M_{\odot}$) form from stars with $M_{\text{ZAMS}} \simeq 62 M_{\odot}$, that is they do not form from the collapse of the most massive stars. This happens because PPISNe significantly enhance the mass loss of stars with $60 \leq M_{\text{ZAMS}} / M_{\odot} \leq 115$ and PISNe cause the disintegration of the stars with $M_{\text{ZAMS}} \gtrsim 120 M_{\odot}$.

From Fig. 5, it is also apparent that most compact remnants distribute along the curve obtained from single stellar evolution calculations (dashed line). These remnants come from binary stars that evolved through no (or minor) mass transfer episodes.

In contrast, primary stars that underwent a Roche lobe overflow episode, or that have lost their envelope after a CE phase, tend to form smaller compact objects than they would have formed if they were evolved as single stars. This is apparent in panels a2, b2, and c2 of Fig. 5, where compact objects formed by primary stars tend to fall below the single stellar evolution curve.

Panel c2 is a particularly significant case: most primaries with ZAMS mass between ~ 25 and $\sim 85 M_{\odot}$ at $Z = 10^{-4}$ become compact remnants with a factor of $\sim 2-3$ lower mass than compact remnants born from single stars with the same ZAMS mass. These primary stars undergo Roche lobe overflow followed by CE

³For primary and secondary star we mean the more massive and the less massive member of the binary in the ZAMS.

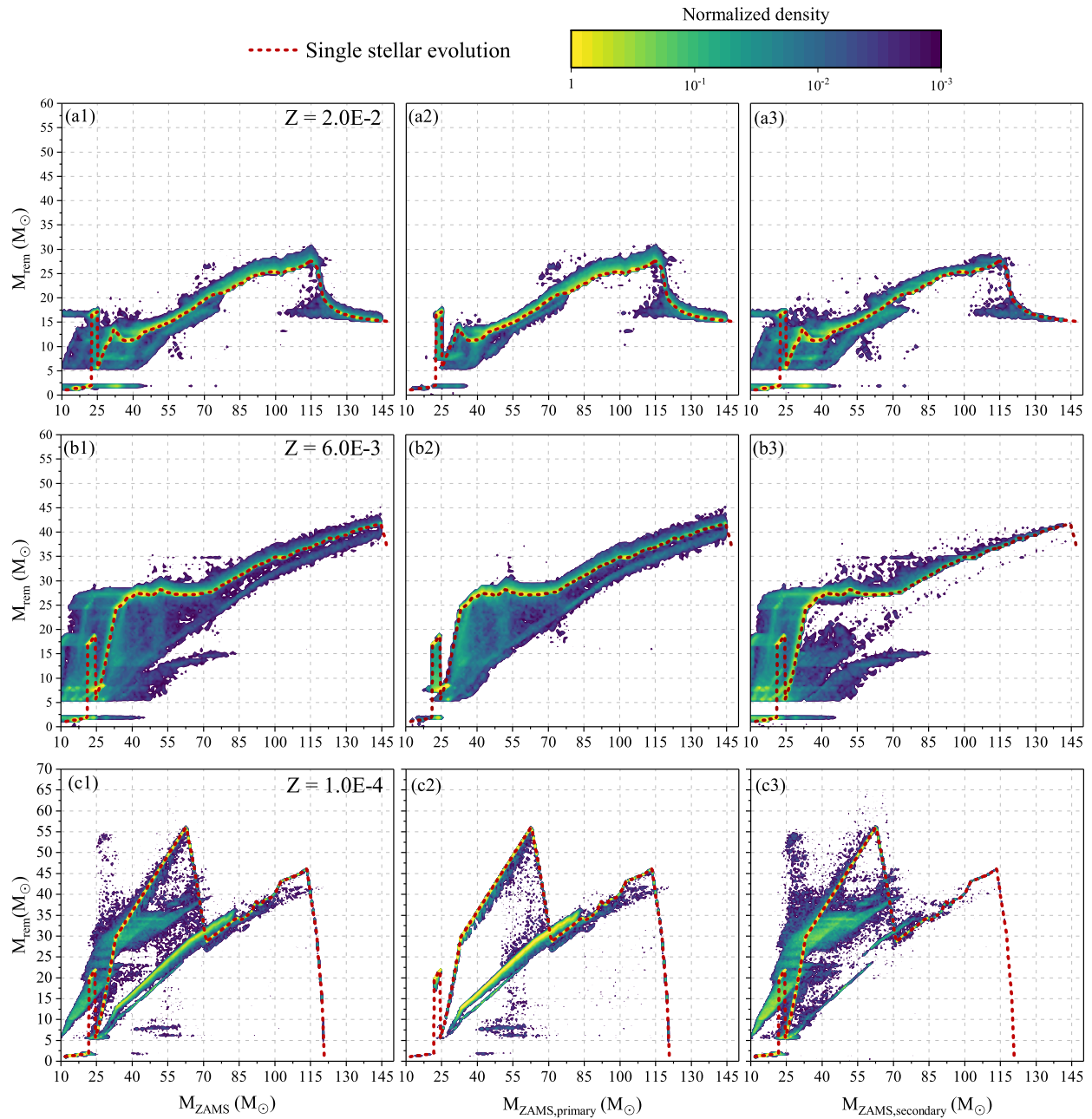


Figure 5. Mass of compact remnants ending up in compact-object binaries, as a function of the ZAMS mass of the progenitor star. The logarithmic colour bar represents the number of compact objects per cell, normalized to the maximum cell-value of each plot. Each cell is a square with a side of $0.5 M_{\odot}$. Rows labelled as *a*, *b* and *c* show the mass spectrum of compact remnants at metallicity $Z = 2 \times 10^{-2}$, $Z = 6 \times 10^{-3}$ and $Z = 10^{-4}$, respectively. Columns labelled as *1* show all compact remnants; columns labelled as *2* (*3*) show only the compact remnants formed from the primary (secondary) star. The dashed line is the mass spectrum of compact objects obtained from single stellar evolution calculations.

evolution and are completely stripped of their Hydrogen envelope, becoming WR stars.

The secondary stars with $M_{\text{ZAMS}} \lesssim 30 M_{\odot}$ that accreted mass from the primary star tend to form more massive compact objects than they would have formed if they were single stars (see panels *a3*, *b3*, and *c3*).

More massive secondaries ($M_{\text{ZAMS}} \gtrsim 30 M_{\odot}$) either fill their Roche lobe at later stages, after they have become more massive than the primary (which has typically evolved into a

compact object) or undergo CE; so they lose significant mass and form compact remnants that fall below the single stellar evolution curve (e.g. panel *b3* for $25 \leq M_{\text{ZAMS}}/M_{\odot} \leq 85$ and $5 \leq M_{\text{rem}}/M_{\odot} \leq 20$).

The deviation from the mass spectrum obtained from single stellar evolution is more pronounced at low metallicity. This happens because stellar winds are quenched at low metallicity; therefore, the mass that can be exchanged during a Roche lobe overflow episode or lost during a CE phase is significantly larger at low Z .

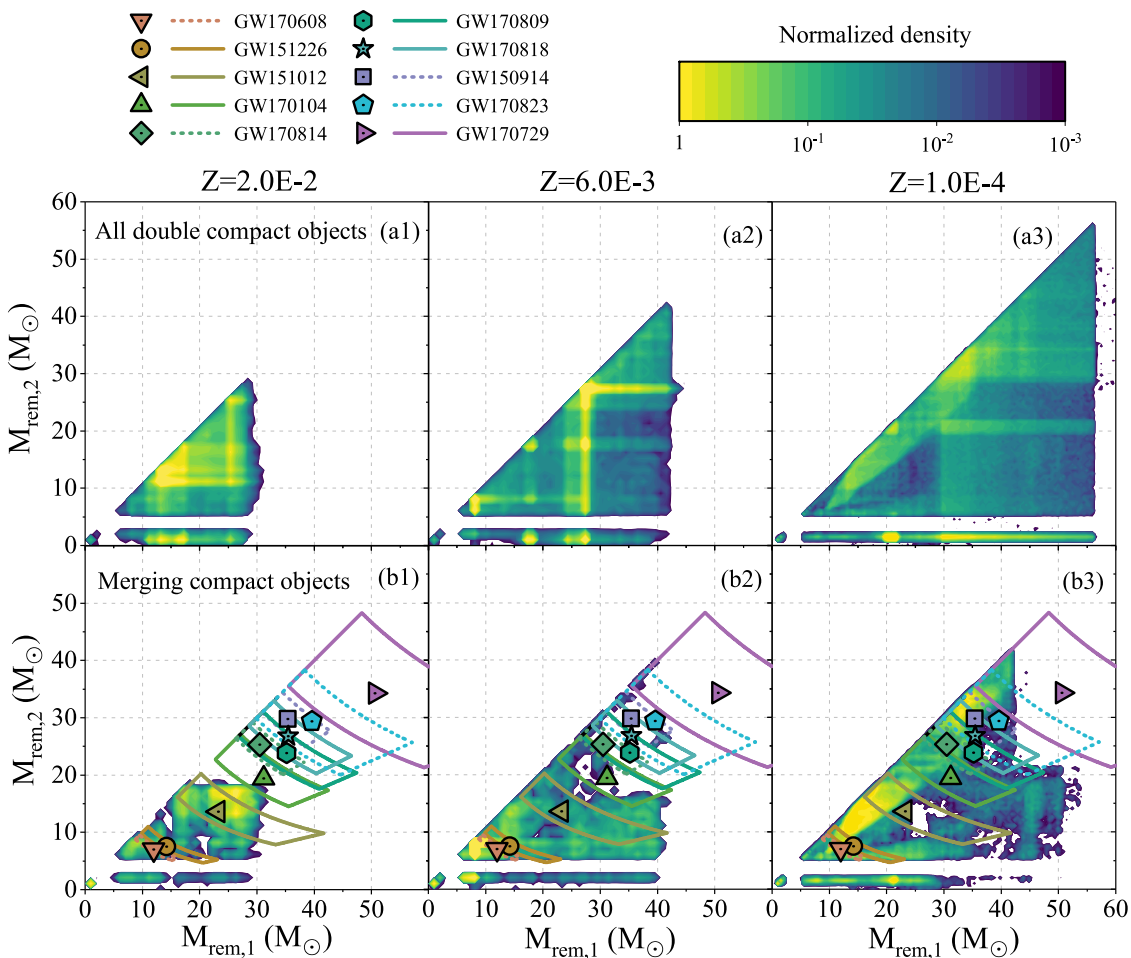


Figure 6. Mass of the less massive remnant ($M_{\text{rem},2}$) as a function of the mass of the more massive remnant ($M_{\text{rem},1}$) in all compact-object binaries (top row, labelled as *a*), and in the compact-object binaries merging within a Hubble time (bottom row, labelled as *b*). The logarithmic colour bar represents the number of remnants per cell, normalized to the maximum cell-value of each plot. Each cell is a square with a side of $0.5 M_{\odot}$. Left-hand column (labelled as *I*): $Z = 2 \times 10^{-2}$; central column (2): $Z = 6 \times 10^{-3}$; right-hand column (3): $Z = 10^{-4}$. The symbols are the BH mergers detected by LIGO/Virgo in O1 and O2. The solid and dashed lines around the symbols define the 90 per cent credible interval on the chirp mass and the mass ratio of each GW event. A version of this figure containing all the other considered metallicities is shown in the supplementary material, Appendix D.

It is also worth noting that the mass range of BHs in compact-object binaries is very similar to that obtained from single stellar evolution calculations. In particular, it is very unlikely to find BHs in binaries with a mass significantly larger than the maximum BH mass obtained from single-star evolution, for every metallicity.

From Fig. 5, it is also apparent that we have a mass gap between the heaviest NS ($\sim 2 M_{\odot}$) and the lightest BH ($\sim 5 M_{\odot}$). This is a feature of the adopted *rapid* SN explosion model that reproduces the observed mass gap between NS and BH masses.

Fig. 6 shows the mass of the less massive remnant as a function of the mass of the more massive remnant, for all double compact-object binaries (*a* panels, in the top row) and for all compact-object binaries merging within a Hubble time (*b* panels, in the bottom row). In the panels of the top row of Fig. 6, we find a large number of BHs in the areas where the mass spectrum of compact remnants from single stars (see the dashed line of Fig. 5) is quite flat. For instance, at $Z = 2 \times 10^{-2}$, all stars with $30 \leq M_{\text{ZAMS}}/M_{\odot} \leq 65$ form BHs with masses between $10 M_{\odot}$ and $17 M_{\odot}$ (cf. panel *a1* of Fig. 5).

Fig. 6 shows that merging BHs with masses consistent with GW151226, GW170608, and GW151012 (i.e. the low-mass GW

events) form at all metallicities in our simulations. GW150914, GW170104, GW170809, GW170814, GW170818, and GW170823 (i.e. the GW events hosting BHs with $M_{\text{BH}} \geq 30 M_{\odot}$) are perfectly matched by the masses of simulated merging BHs at low metallicity ($Z = 10^{-4}$, panel *b3*), while merging BHs with mass $> 20 M_{\odot}$ do not form in our simulations at $Z = 2 \times 10^{-2}$. The 90 per cent credible levels for the masses of GW150914, GW170104, GW170809, GW170814, GW170818, and GW170823 partially overlap with our simulated merging BHs at $Z = 6 \times 10^{-3}$ (see panels *b1* and *b2*, respectively). From Fig. 6, it is also apparent that it is unlikely to find merging BHs with masses consistent with GW170729 (i.e. the GW event with the heaviest BHs). The 90 per cent credible levels for the masses of GW170729 partially overlap with our merging BHs only at $Z = 10^{-4}$. On the other hand, dynamical processes might easily lead to the formation of GW170729-like systems (Di Carlo et al. 2019).

It is also worth noting that the most massive BHs formed in our simulations are unlikely to merge within a Hubble time via GWs. Specifically, at $Z = 2 \times 10^{-2}$ we do form compact-object binaries with both BHs more massive than $\sim 20 M_{\odot}$ (upper-triangular area of panel *a1*) but they do not merge via GWs (the same triangular

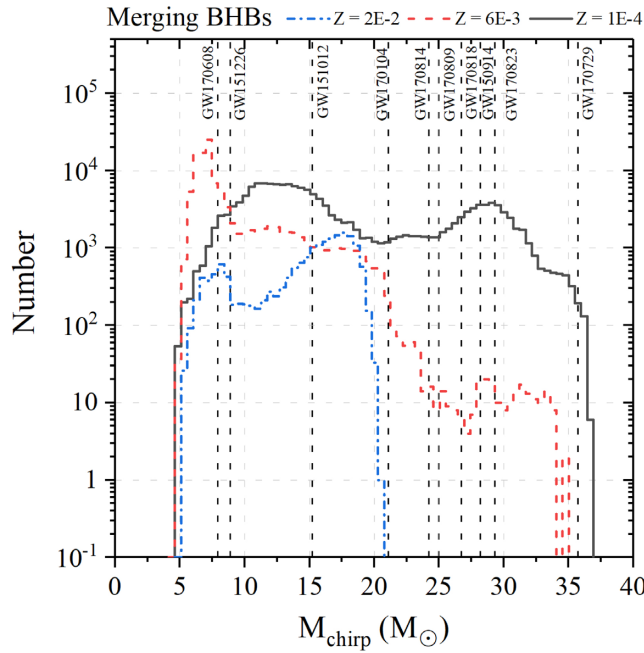


Figure 7. Chirp mass distributions of merging BHBs. The different lines show the results at different metallicities. Dash-dotted blue line: $Z = 2 \times 10^{-2}$; dashed red line: $Z = 6 \times 10^{-3}$; solid black line: $Z = 10^{-4}$. The vertical dashed lines represent the chirp masses of the GW detections. From left to right: GW170608, GW151226, GW151012, GW170104, GW170814, GW170809, GW170818, GW150914, GW170823, and GW170729. A version of this figure containing all the other considered metallicities is shown in the supplementary material, Appendix D.

area is missing in panel *b1*). We obtain the same result at $Z = 6 \times 10^{-3}$ for BHs with mass $\gtrsim 25 M_{\odot}$ and at $Z = 10^{-4}$ for BHs with mass $\gtrsim 40 M_{\odot}$.

Fig. 7 shows the distribution of the chirp masses of merging BHBs at different metallicity. It is apparent that merging BHBs with $M_{\text{chirp}} \gtrsim 20 M_{\odot}$ (such as GW150914 and GW170814) cannot form at $Z = 2 \times 10^{-2}$. Merging BHBs with $20 \leq M_{\text{chirp}} \leq 35$ are also unlikely to form at $Z = 6 \times 10^{-3}$, while they are quite common at $Z \lesssim 10^{-4}$. Furthermore, in our simulations we do not find merging BHs with $M_{\text{chirp}} \gtrsim 37 M_{\odot}$, independently of metallicity.

Fig. 8 shows the distribution of the mass ratio ($q = \frac{M_2}{M_1}$, $M_1 \geq M_2$) of merging BHBs. At all metallicities, most merging BHs have $q > 0.5$, but the fraction of systems with lower mass ratio is not negligible, especially at low Z where the merging BHs with $q < 0.5$ are ~ 10 per cent of the total. We do not find merging BHs with $q < 0.1$, and very low mass ratios ($0.1 < q < 0.2$) seem to be possible only at low metallicity. From Fig. 8, it is also apparent that we match the mass ratios of GW detections at all the considered metallicities.

4 DISCUSSION

4.1 Dearth of massive BHB mergers

We have shown in Section 3 that the BHBs with the heaviest BH members are unlikely to merge within a Hubble time (see Fig. 6). This happens because the separation of two massive BHs at the time of the formation of the second remnant is generally too large to let the BHs merge via GWs. This is apparent from Fig. 9, which shows the semimajor axis of double compact objects at the time of the formation of the second remnant as a function of the mass of

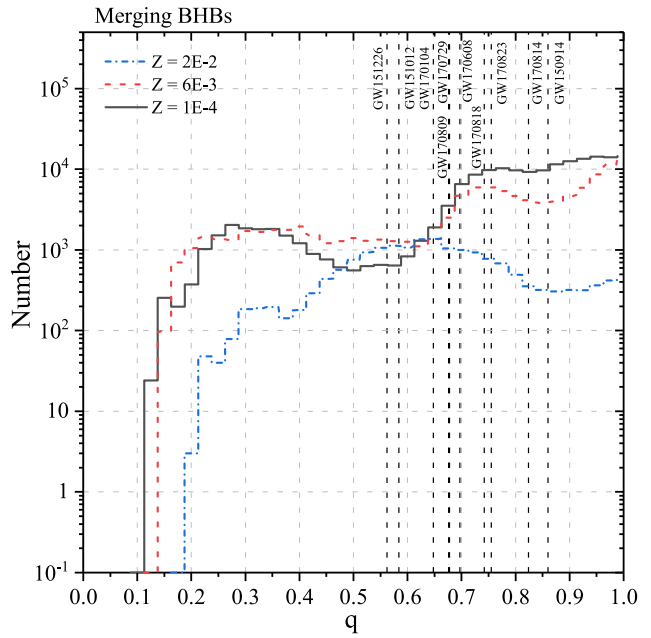


Figure 8. Distribution of the mass ratio of merging BHBs. The different lines show the results at different metallicities. Dash-dotted blue line: $Z = 2 \times 10^{-2}$; dashed red line: $Z = 6 \times 10^{-3}$; solid black line: $Z = 10^{-4}$. The vertical dashed lines represent the mass ratio the GW detections. From left to right: GW151226, GW151012, GW170104, GW170729, GW170809, GW170608, GW170818, GW170823, GW170814, and GW150914. A version of this figure containing all the other considered metallicities is shown in the supplementary material, Appendix D.

the less massive compact object. At all metallicities, most of the heaviest BHs have quite large semimajor axes ($a > 10^2 R_{\odot}$, grey points).

To better understand the evolution of massive BHBs, we extract from our simulations all the binaries that would have formed the most massive BHs if we had accounted only for single stellar evolution. We select them by looking at the zones of avoidance of massive merging BHs shown in the bottom row panels of Fig. 6 and already described in Section 3. Fig. 10 shows the mass of the less massive remnant as a function of the mass of the more massive remnant for such binary systems. The left-hand column shows the BHBs we obtain if we account only for single stellar evolution. The other two columns show the BHBs formed when including also binary stellar evolution processes. In particular, the central column shows the non-merging BHBs while the right-hand column shows the merging BHBs.

From Fig. 10 it is apparent that merging BHs tend to be lighter than we would have expected evolving their progenitors through single stellar evolution. The area filled by BHs in the left-hand column of Fig. 10 is mostly empty in the right-hand column.

Two massive progenitor stars may

- (i) merge during the MS phase, if they are born too close to each other ($a \lesssim 50 R_{\odot}$);
- (ii) evolve through no (or minor) mass-transfer episodes if they are born too far away from each other ($a \gtrsim \text{few } 10^3 R_{\odot}$);
- (iii) interact significantly with each other if $a \in [50 R_{\odot}; 10^3 R_{\odot}]$.

In the first case, the stars merge and form one single massive star. In the second case, the progenitor stars do form a double compact object but the remnants do not merge within a Hubble time because

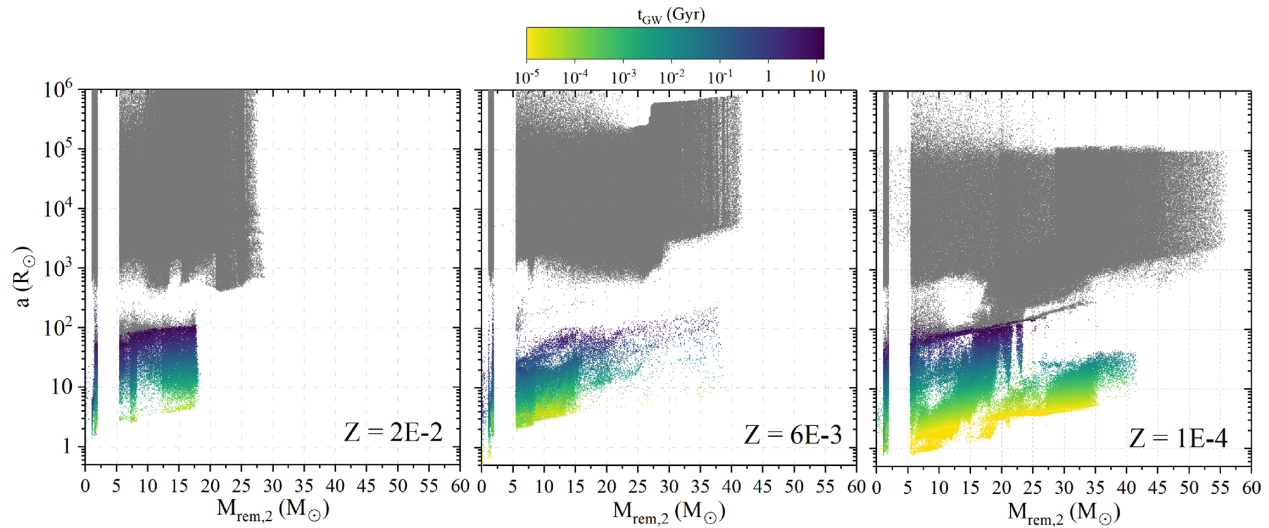


Figure 9. Semimajor axis as a function of the mass of the less massive remnant in double compact-object binaries. The semimajor axis is taken at the time of the formation of the second compact remnant. Left-hand panel (a): $Z = 2 \times 10^{-2}$; central panel (b): $Z = 6 \times 10^{-3}$; right-hand panel (c): $Z = 10^{-4}$. The logarithmic colour bar represents the GW merger time-scale (Peters 1964). Grey points show the systems that do not merge within a Hubble time.

the semi-major axis is too large (most of the systems in the central column of Fig. 10 belong to this category). In the third case, the progenitor stars may form a merging BHB (right-hand column of Fig. 10).

At low metallicity (bottom row of Fig. 10) stellar winds are quenched, therefore the heaviest BHs should come from progenitor stars with large radii ($\gtrsim 10^3 R_\odot$) and massive Hydrogen envelopes ($\gtrsim 20 M_\odot$). When such stars interact with each other, a stable Roche lobe mass transfer phase and/or a CE evolution may significantly shrink the binary system so that $a \lesssim 10^2 R_\odot$ and the BHs merge within a Hubble time. Still, most of the massive Hydrogen envelopes are lost during Roche lobe overflow and CE, therefore the resulting BHs are significantly lighter than those formed considering only single stellar evolution. This effect is particularly strong at low Z and for massive progenitor stars, that is for stars with massive Hydrogen envelopes.

It is also worth noting that a merging BHB with high mass ratio can form if a binary system evolves through a stable Roche lobe mass transfer (or CE phase) when one of the two stars has already turned into a BH (panel *c3* of Fig. 10 for $M_{\text{rem},1} \gtrsim 40 M_\odot$ and $M_{\text{rem},2} \lesssim 20 M_\odot$). In contrast, equal-mass merging BHs may form if the progenitor stars undergo a stable Roche lobe mass transfer followed by a CE phase (less likely a double CE evolution) and transform into two bare-He cores. Our stellar evolution prescriptions at $Z = 10^{-4}$ predict that the maximum BH mass that can result from a bare-He star is $\sim 40 M_\odot$. This explains the cut-off at $M_{\text{rem},1} \simeq 40 M_\odot$ observed in panel *c3* of Fig. 10 and in panel *b3* of Fig. 6.

At high metallicity, the situation is quite different. From single stellar evolution calculations we know that the heaviest BHs should form from WR stars, that is stars with small radii (few R_\odot) and without a Hydrogen envelope (lost through stellar winds). In our models, at $Z = 2 \times 10^{-2}$, most of massive progenitors have always $R \lesssim 10^2 R_\odot$ during their life (cf. panel *b1* of Fig. 3), therefore they are unlikely to interact with each other because they are quite small. This implies that a BHB formed from such progenitors unlikely becomes tight enough to merge within a Hubble time. To obtain tighter BHBs, we need lighter progenitor stars, that is stars that expand significantly before turning into bare-He stars, so that they can evolve through a CE phase. This also explains why in panel

a3 of Fig. 10 we have only dark-blue points, that is quite light merging BHs ($M_{\text{rem},2} \lesssim 20 M_\odot$) that come only from relatively light progenitors ($M_{\text{ZAMS}} \lesssim 75 M_\odot$).

At $Z = 6 \times 10^{-3}$ the situation is intermediate. Most of the heaviest BHs are still expected to come from WR stars but their progenitors may reach quite large radii ($\gtrsim 10^2 R_\odot$) before turning into bare-He cores. Some of these progenitors may still evolve through a CE phase but the binary system cannot shrink significantly because the Hydrogen envelopes are too light ($< 10 M_\odot$). This also explains why in panel *b3* of Fig. 10 we have only very few points with $M_{\text{rem},2} \gtrsim 25 M_\odot$. Merging BHs can still form after a CE evolution provided that the shared envelope is quite massive ($\gtrsim 10 M_\odot$), but in this case at least one of the two BHs must be quite light, as already discussed for the low- Z case.

4.2 Number of BH mergers

Stellar winds and stellar radii are crucial ingredients to understand how the number of merging BHs depends on metallicity. At high Z , the semimajor axis of binary stars may easily increase because of strong stellar winds, therefore BHBs tend to have larger separations. Furthermore, the most massive stars ($M_{\text{ZAMS}} \gtrsim 75 M_\odot$ at $Z = 2 \times 10^{-2}$) lose all their Hydrogen envelope via stellar winds without turning into supergiants. This means that metal-rich stars have also less chances to interact with each other because WR stars have quite small radii. Even though lighter stars ($M_{\text{ZAMS}} \lesssim 75 M_\odot$ at $Z = 2 \times 10^{-2}$) may undergo a CE phase, the shared envelope is likely quite light (because stellar winds removed a large fraction of the envelope), therefore metal-rich stars have also less mass reservoir that can be used to shrink binary systems.

For these reasons, we expect a higher number of BH mergers at low metallicity, where stellar winds are quenched and stars can reach larger radii and retain more massive envelopes. Fig. 11 confirms the expectations. It shows the number of merging BHs per unit stellar mass in our simulations ($N_{\text{cor}, \text{BHB}}$, bottom panel) and the number of WR stars per unit stellar mass (top panel) predicted by our single stellar evolution models, as a function of metallicity.

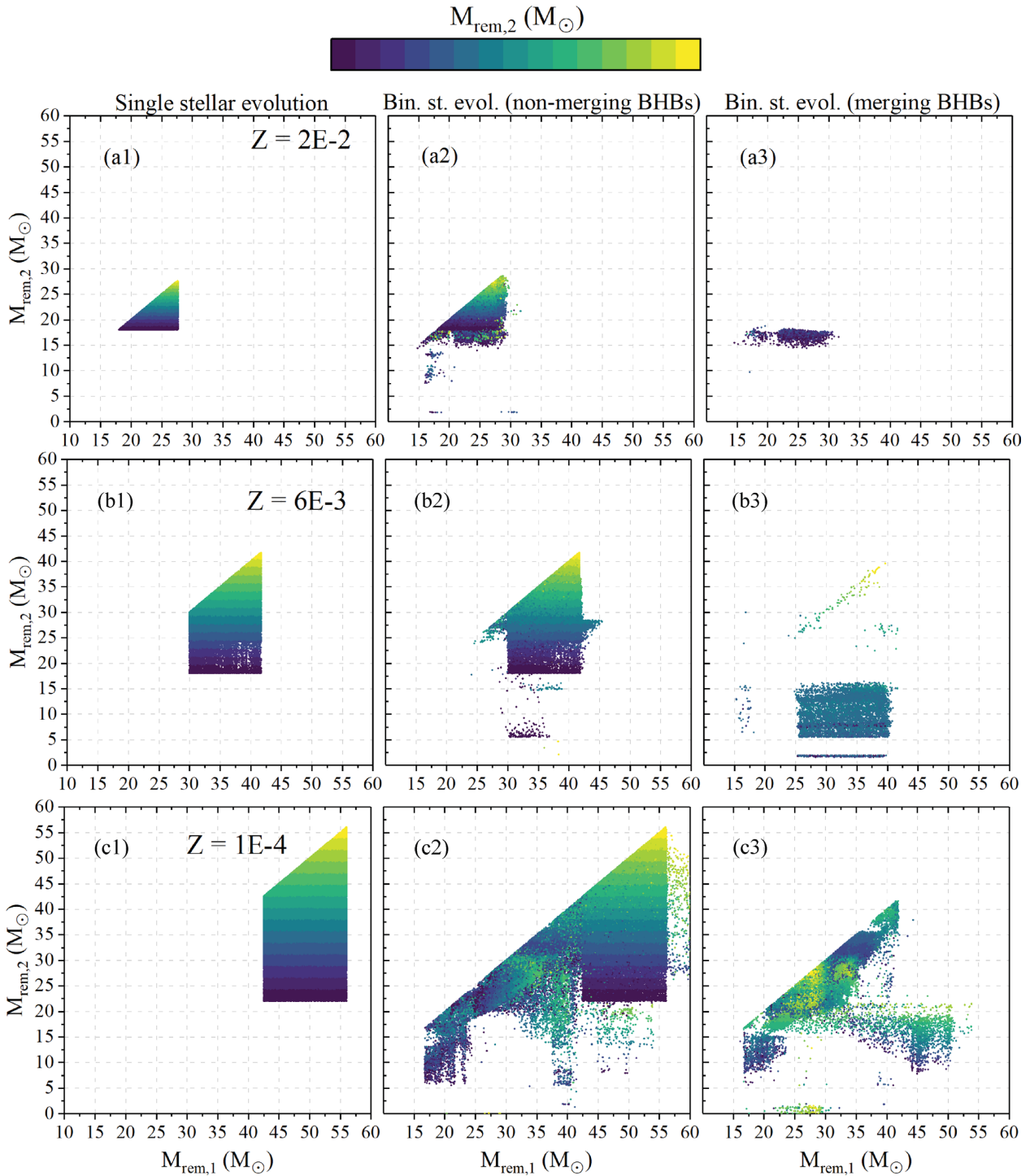


Figure 10. Mass of the less massive remnant ($M_{\text{rem},2}$) as a function of the mass of the more massive remnant ($M_{\text{rem},1}$) for the subset of double compact-object binaries that would form the heaviest BHs if we accounted only for single stellar evolution calculations. Left-hand column (labelled as 1): compact-object binaries that form if we account only for single stellar evolution processes; central column (labelled as 2): non-merging compact-object binaries that form if we account for both single and binary stellar evolution processes in our population-synthesis simulations; right-hand column (labelled as 3): same as in the central column but for merging binaries. Panels in the top row (labelled as *a*): $Z = 2 \times 10^{-2}$; central row (*b*): $Z = 6 \times 10^{-3}$; bottom row (*c*): $Z = 10^{-4}$. Colours show the value of the mass of the less massive remnant obtained from single stellar evolution (i.e. the values of $M_{\text{rem},2}$ in the left-hand column).

We compute $N_{\text{cor, BHB}}$ following the formula given in Giacobbo et al. (2018):

$$N_{\text{cor, BHB}} = f_{\text{bin}} f_{\text{IMF}} \frac{N_{\text{mergers, BHB}}}{M_{\text{tot}}}, \quad (25)$$

where $N_{\text{mergers, BHB}}$ is the number of merging BHs, M_{tot} is the total initial mass of the simulated stellar population, f_{IMF} corrects for the fact that we have simulated only stars with ZAMS mass $M_{\text{ZAMS}} \geq 10 M_{\odot}$ ($f_{\text{IMF}} = 0.137$), and f_{bin} is a correction factor which accounts

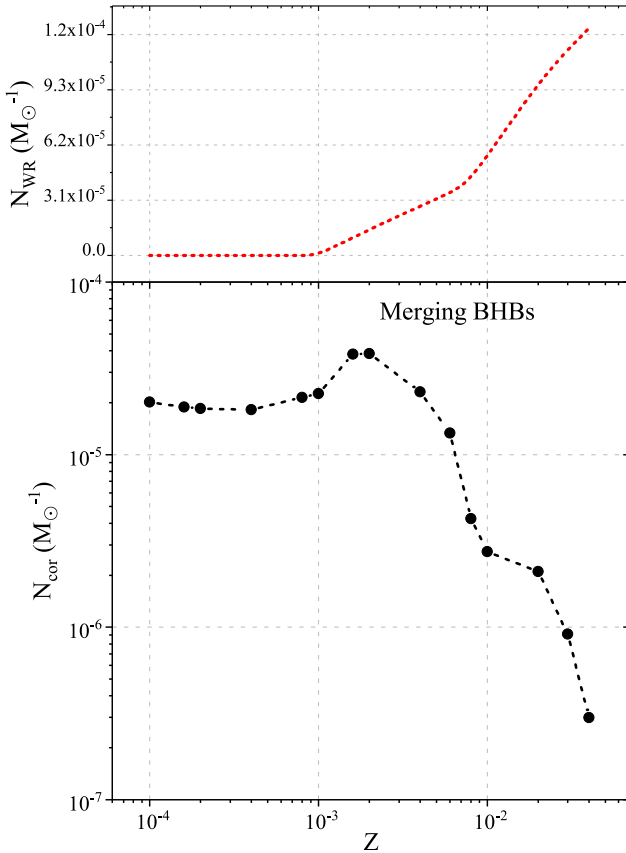


Figure 11. Top panel: number of WR stars per unit mass predicted by the SEVN code, as a function of metallicity. The data have been obtained for the stellar population used in our simulations and considering only single stellar evolution processes. Bottom panel: number of merging BHs per unit mass as a function of metallicity.

for the fact that all stars in our sample are members of binary systems. To compute $N_{\text{cor}, \text{BHB}}$ we assume that only 50 per cent of stars are binaries (Sana et al. 2013), that is $f_{\text{bin}} = 0.5$. Fig. 11 shows a peak of BH mergers at $Z \simeq 3 \times 10^{-3}$, which corresponds to the lowest metallicity at which massive single stars can evolve into WR stars (top panel, dashed red curve).

Fig. 11 also shows a mild decrease of the number of merging BHs at $Z \lesssim 2 \times 10^{-3}$. At $Z = 2 \times 10^{-3}$ we have a factor of ~ 3 more merging BHs than at $Z = 10^{-4}$. The onset of PISNe plays only a minor role: PISNe disrupt the progenitors of heavy BHs before they can form a remnant, reducing the number of BHs at low metallicity; on the other hand, only the most massive stars ($M_{\text{He}} \gtrsim 60 M_{\odot}$) explode as PISNe, thus their impact on $N_{\text{cor}, \text{BHB}}$ is negligible.

The decrease of $N_{\text{cor}, \text{BHB}}$ at $Z \leq 2 \times 10^{-3}$ mainly happens because we form significantly more BHs at $Z = 2 \times 10^{-3}$ than at $Z = 10^{-4}$. In our simulations, binary stars with members with $M_{\text{ZAMS}} \in [15; 30] M_{\odot}$ (which produce a large fraction of all double compact objects) form more or less the same number of double compact objects at $Z = 2 \times 10^{-3}$ and $Z = 10^{-4}$ ($\sim 1.5 \times 10^5$ double compact objects). The vast majority of these double compact objects at $Z = 10^{-4}$ are BH-NS binaries ($\sim 1.1 \times 10^5$), while the number of BHs is 2×10^4 and only ~ 1000 of them merge within a Hubble time. We obtain the same result if we evolve the same systems considering only single stellar evolution calculations.

In contrast, at $Z = 2 \times 10^{-3}$, we find $\sim 1.1 \times 10^5$ BHs ($\sim 2 \times 10^4$ of them merge within a Hubble time), and only $\sim 4 \times 10^4$ BH-NS systems.

The evolution of the considered progenitor stars is similar at both $Z = 2 \times 10^{-3}$ and $Z = 10^{-4}$: double compact objects form after a CE phase involving a BH (formed from the primary star) and the secondary star. The difference is that at $Z = 2 \times 10^{-3}$, the primary star, before turning into a BH, fills the Roche lobe and the system evolves through a stable mass transfer phase. In this case, the mass transferred from the primary star is enough to let the secondary star form a BH instead of a NS, after the CE evolution. In contrast, at $Z = 10^{-4}$, progenitor stars have smaller radii, therefore the considered binary systems do not evolve through a stable mass-transfer phase before entering CE.

It is also worth noting that at $Z = 2 \times 10^{-3}$ the secondary star undergoes the CE evolution when it is in the core-Helium burning phase, whereas at $Z = 10^{-4}$ the star has already formed a CO core and it has Helium and Hydrogen in the outer shells.

The reason of this difference is that, according to PARSEC evolutionary tracks,⁴ stars with $M_{\text{ZAMS}} \in [15; 30] M_{\odot}$ and metallicity $Z = 2 \times 10^{-3}$ ignite Helium as red supergiant stars. Such stars have quite large radii and likely undergo a CE phase during the He-core burning phase.

In contrast, stars with the same mass ($M_{\text{ZAMS}} \in [15; 30] M_{\odot}$) and metallicity $Z = 10^{-4}$ ignite Helium as yellow/blue supergiants, which means that they are not large enough to evolve through a CE phase at that stage. Such stars can enter CE only when they turn into red supergiant stars, that is, when they have already formed a CO core.

4.3 Local merger rate density

We use the results of our simulations to estimate the local merger rate density of BHs ($R_{\text{loc}, \text{BHB}}$) and we compare it with the rate inferred from the LIGO-Virgo data.

To calculate the merger rate density of BHs in the local Universe (R_{BHB}) we adopt the simple analytic calculation described in Section 3.5 of Giacobbo & Mapelli (2018):

$$R_{\text{BHB}} = \frac{1}{H_0 t_{\text{lb}}(z=0.1)} \int_{z_{\text{max}}}^{z_{\text{min}}} \frac{f_{\text{loc}}(z) \text{SFR}(z)}{(1+z) [\Omega_M (1+z)^3 + \Omega_\Lambda]^{1/2}} dz, \quad (26)$$

where SFR(z) is the star formation rate density as a function of redshift (we adopt the fitting formula provided in Madau & Dickinson 2014), $t_{\text{lb}}(z=0.1)$ is the look back time at redshift $z = 0.1$, $f_{\text{loc}}(z)$ is the fraction of binaries which form at redshift z and merge in the local Universe (defined as $z \leq 0.1$), $z_{\text{max}} = 15$, $z_{\text{min}} = 0$, while H_0 , Ω_M , and Ω_Λ are the cosmological parameters (for which we adopt values from Planck Collaboration et al. 2016).⁵

We calculate $f_{\text{loc}}(z)$ from $N_{\text{cor}, \text{BHB}}$ (equation 25), assuming that all stars in the same redshift bin have the same metallicity. We compute

⁴Stellar radii are crucial to understand when the secondary star evolves through a CE phase. In this respect, it is important to remind that the evolution of massive stars in the HR diagram, after central Hydrogen burning, strongly depends on the details of the input physics (Chiosi & Summa 1970; Tang et al. 2014). Stars with relatively lower mass undergo a very similar evolution to intermediate mass stars, reaching central He ignition in the red supergiant region. In more massive stars, however, it is possible that central Helium ignition happens already in the blue/yellow supergiant phase.

⁵Note that equation (26) is the same as equation (10) of Giacobbo & Mapelli (2018), but is written as an integral rather than a summation.

the metallicity at a given redshift as $\log Z(z)/Z_\odot = -0.19z$ if $z \leq 1.5$ and $\log Z(z)/Z_\odot = -0.22z$ if $z > 1.5$. This formula comes from abundance measurements of a large sample of high-redshift damped Ly α systems (Rafelski et al. 2012), but re-scaled to have $Z(z=0) = Z_\odot$, consistent with the Sloan Digital Sky Survey data (Gallazzi et al. 2008).

Our model predicts $R_{\text{loc},\text{BHB}} \simeq 90 \text{ Gpc}^{-3} \text{ yr}^{-1}$, consistent with the BHB merger rate inferred from LIGO–Virgo data (24–112 $\text{Gpc}^{-3} \text{ yr}^{-1}$ Abbott et al. 2018a,b)

4.4 Formation of massive single BHs

We have shown in Section 3 (Fig. 4) that while the mass distribution of BHs that are members of double compact objects is similar to the one obtained from single stellar evolution, the mass distribution of single BHs is quite peculiar, especially at low metallicity. We know that PPISNe significantly enhance mass loss from massive progenitor stars and PISNe disrupt massive stars before they can form a heavy BH. Thus, from single stellar evolution, we do not expect to form BHs with mass $\gtrsim 60 M_\odot$ (Spera & Mapelli 2017).

In contrast, if we account for binary evolution processes, we can form single BHs with mass up to ~ 65 , 90 , and $145 M_\odot$ at $Z = 2 \times 10^{-2}$, 6×10^{-3} , and 10^{-4} , respectively. In our simulations, such heavy BHs may form from the merger of two MS stars when one of them is at the end of the MS phase. In this case, the SEVN code assumes that the merger product is also at the end of the MS phase. Even if the merger product has a significant amount of Hydrogen, we assume that most of it is part of the envelope; therefore, it will not be transformed into Helium by nuclear reactions. This implies that the mass of the Helium core of the merger product may be lower than the limit for a PISN to occur. Thus, the merger product can form a BH by direct collapse, and such BH can be very massive, considering the large mass of the Hydrogen envelope.

This effect is more pronounced at low metallicity where stellar winds are not strong enough to remove the massive Hydrogen envelope of the merger product. Since such massive BHs are single and very rare ($\lesssim 0.1$ per cent of the total number of BHs at $Z = 10^{-4}$) they do not play a major role in binary population-synthesis simulations. In contrast, they can be very important if they form in star clusters, where they have a high chance to acquire a companion through dynamical exchanges, so that they possibly become loud GW sources (Portegies Zwart & McMillan 2000; Mapelli 2016; Askar et al. 2017).

4.5 Comparison with COMBINE

Recently, Kruckow et al. (2018) used a new grid-based population synthesis code (COMBINE) to study the formation and evolution of double compact-object binaries. In this section we discuss the main differences between SEVN and COMBINE.

Both codes interpolate look-up tables to evolve the physical parameters of single stars. Furthermore, they both use similar criteria to jump on new tracks whenever a star has accreted (donated) a significant amount of mass from (to) its companion. The main differences in the interpolation scheme are:

(i) COMBINE interpolates only on the mass variable while SEVN interpolates also over different metallicities. This means that with SEVN we can evolve stars at any metallicity between $Z = 10^{-4}$ and $Z = 4 \times 10^{-2}$;

(ii) COMBINE uses linear weights to interpolate tracks (see equations (A1) and (A2) of Kruckow et al. 2018), while in SEVN we use

more sophisticated weights that significantly improve interpolation errors (see equations (A3) and (A4) and Spera & Mapelli (2017) for details);

(iii) To calculate the interpolation time for the stellar tracks, COMBINE uses the ratio between the current age of a star and its total lifetime (see eq. A6 of Kruckow et al. 2018), while in SEVN we improve the accuracy of the interpolation by using the relative age of a star with respect to its current evolutionary phase (see Section 2.1.1 and Appendix A).

The main difference in terms of scientific results is that COMBINE matches the low-mass GW events (GW151226 and GW170608) only at high metallicity (see fig. 15 of Kruckow et al. 2018), while with SEVN we can form such events at all metallicities (see Fig. 6). This happens because the two codes use different prescriptions for the formation of BHs. In COMBINE, a BH forms if the final CO core mass of a star is $> 6.5 M_\odot$ and the BH mass is calculated assuming a fixed amount of fallback (80 per cent of the mass of the He envelope). This implies that, at high metallicity, COMBINE forms BHs with mass $\gtrsim 6.5 M_\odot$ (see Fig. 2 of Kruckow et al. (2018)). At low metallicity, stellar winds are quenched, therefore stars have more massive He envelopes and the minimum BH mass is larger ($\gtrsim 10 M_\odot$). In contrast, in our work, we adopt the rapid SN explosion model (Fryer et al. 2012), which predicts variable fallback and does not distinguish a priori between NSs and BHs. We impose that all compact objects with mass $\geq 3 M_\odot$ are BHs while the others are NSs. As a consequence, in SEVN we can form smaller BHs (down to $\sim 5 M_\odot$) from the collapse of stars with final CO core masses of $\sim 4 M_\odot$, and with small fallback fractions (~ 5 per cent). Furthermore, our minimum BH mass is quite insensitive to metallicity because BHs of $\sim 5 M_\odot$ form from stars with $M_{\text{ZAMS}} \simeq 25 M_\odot$ whose final physical parameters mildly depend on metallicity.

The difference in the maximum BH mass at high metallicity (~ 11 and $35 M_\odot$ in ComBinE and SEVN, respectively) is also a consequence of the different SN explosion prescriptions adopted by the two codes. At low metallicity, both SEVN and COMBINE form BHs with mass up to $\sim 60 M_\odot$ (see Fig. 7 of Kruckow et al. 2018 and our Fig. 6). Still, while the $60 M_\odot$ cut-off in SEVN comes from PPISNe and PISNe, the latter are not included in COMBINE. The inclusion of PPISNe and PISNe would significantly reduce the maximum BH mass obtained by COMBINE at low metallicity.

Other differences come from binary stellar evolution prescriptions. For example, the prescriptions for BH natal kicks are quite different in the two codes. COMBINE adopts a flat distribution of BH natal kicks between 0 and 200 km/s , while SEVN assumes the Hobbs et al. (2005) distribution ($\sigma_{\text{ID}} = 265 \text{ km/s}$) scaled by the amount of fallback mass (see Section 2.2). Furthermore, both codes adopt the $\alpha\lambda$ -formalism for the common envelope phase, but COMBINE calculates the λ parameter directly from the stellar structure, while SEVN still assumes a fixed λ (we use $\lambda = 0.1$ for this paper). We will improve this aspect in the next version of SEVN. Finally, wind accretion and tidal evolution are not included in COMBINE. Simultaneous circularization is assumed by COMBINE when the binary is at the onset of Roche lobe mass transfer. Furthermore, in COMBINE, the donor star is always assumed to transfer its envelope entirely to the accretor, while in SEVN we limit mass loss by taking into account of several factors (see our equations (7–8)).

Overall, SEVN and COMBINE both share the same novel approach (which consists in interpolating stellar evolution from look-up tables), but they have also important differences in the

interpolation algorithm, in the implementation of binary evolution processes and, more importantly, in the formation of compact remnants. This leads to a significantly different mass spectrum of merging BHs, although the results of both codes are still fairly consistent with GW detections.

5 CONCLUSIONS

We investigated the statistics of BHs using a new version of the SEVN population-synthesis code (Spera et al. 2015; Spera & Mapelli 2017). To compute the evolution of physical stellar parameters, SEVN interpolates a set of tabulated stellar evolutionary tracks on-the-fly. The default look-up tables come from the PARSEC stellar evolution code (Bressan et al. 2012; Chen et al. 2015). SEVN also includes five different models for core-collapse SNe and prescriptions to model PPISNe and PISNe. We updated the SEVN code by adding binary stellar evolution processes (wind mass transfer, Roche lobe mass transfer, common envelope, mergers, tides, and GW decay). We also developed a novel algorithm to couple the interpolation of the look-up tables with the binary stellar evolution formulas (supplementary material, Appendix A).

We used the new version of the SEVN code to run 15 sets of simulations with 15 different metallicities ($Z \in [10^{-4}; 4 \times 10^{-2}]$). Each simulation evolves a sample of 10^7 binary systems until all stars have turned into compact remnants.

We found that the mass distribution of BHs which are members of compact-object binaries is quite similar to the one obtained considering only single stellar evolution calculations (Figs. 4 and 5). The maximum BH mass in binary systems is $\sim 30, 45$ and $55 M_{\odot}$ at metallicity $Z = 2 \times 10^{-2}, 6 \times 10^{-3}$, and 10^{-4} , respectively.

In contrast, the mass distribution of single BHs is very different. We form single BHs with mass up to $\sim 65, 90$, and $145 M_{\odot}$ at metallicity $Z = 2 \times 10^{-2}, 6 \times 10^{-3}$, and 10^{-4} , respectively. Such massive BHs fall right into the BH mass-gap ($60 - 120 M_{\odot}$) produced by PPISNe and PISNe (Belczynski et al. 2016b; Spera & Mapelli 2017; Woosley 2017). These heavy BHs come from the merger of two MS stars when one of the two stars is at the end of MS. While these BHs are very rare ($\lesssim 0.1$ per cent of all BHs at $Z = 10^{-4}$), they may be important if they form in star clusters, where they have a high chance to acquire a companion via dynamical exchanges and to become GW sources.

In our simulations, the BHs hosting the heaviest BHs are unlikely to merge within a Hubble time, in agreement with Giacobbo et al. (2018). We found no merging BHs with both BHs more massive than $\sim 18, 25$, and $40 M_{\odot}$ at $Z = 2 \times 10^{-2}, 6 \times 10^{-3}$ and 10^{-4} , respectively. Stellar radii and Hydrogen envelopes play a crucial role to explain why the most massive BHs do not merge (e.g. panel *b1* of Fig. 3). In particular, at low metallicity, the progenitors of the heaviest BHs reach quite large radii ($\gtrsim 10^3 R_{\odot}$) and retain massive Hydrogen envelopes ($\gtrsim 20 M_{\odot}$). When such massive stars evolve through a stable Roche lobe mass transfer or a CE evolution, the orbit shrinks and the massive Hydrogen envelopes are lost. Thus, the BHs formed from massive metal-poor progenitors likely merge within a Hubble time via GWs but they are also quite light, because of the mass lost during CE.

At high metallicity, the progenitors of the heaviest BHs are WR stars, that is stars with small radii (a few R_{\odot}) and no Hydrogen envelopes. This means that such progenitors are unlikely to enter CE and to get close enough to each other to merge within a Hubble time (Figs. 6 and 10).

For similar reasons, merging BHs form more efficiently from metal-poor than from metal-rich progenitors: we expect BH mergers

to be two orders of magnitude more frequent from stars with $Z \leq 2 \times 10^{-3}$ than from solar metallicity stars. This happens because metal-rich stars tend to have small radii and to develop light envelopes (if any), because of the strong stellar winds. With such small radii and envelopes, they can hardly enter a CE phase and they fail to reduce their orbital periods.

The number of merging BHs is maximum for metallicity $Z \sim 2 \times 10^{-3}$, while it drops at higher metallicity and it decreases by a factor of ~ 3 at lower metallicity. If the star metallicity is very low ($Z < 10^{-3}$), we tend to form more BH-NS binaries than BHs, therefore the number of merging BHs decreases slightly with respect to $Z \sim 2 \times 10^{-3}$. This happens because, at $Z \sim 2 \times 10^{-3}$, primary stars with $M_{\text{ZAMS}} \in [20; 30] M_{\odot}$ can evolve through a stable mass-transfer phase and the secondary star ($M_{\text{ZAMS}} \in [15; 25] M_{\odot}$) may acquire enough mass to form a BH instead of a NS. In contrast, at very low metallicity the mass-transfer phase is more unlikely to happen because stars have smaller radii.

Finally, we compared our results against LIGO–Virgo detections. In our simulations, we found that merging BHs with masses consistent with the low-mass GW events (GW151226, GW170608, and GW151012) can form at all metallicities. In contrast, merging BHs consistent with the GW events with primary BH mass $> 30 M_{\odot}$ form only from metal-poor progenitors (Figs. 6, 7, 8). We also found that it is unlikely to form merging BHs with masses consistent with GW170729 (i.e. the GW event with the heaviest BHs). We do not form merging BHs with $M_{\text{chirp}} \gtrsim 37 M_{\odot}$, independently of metallicity. This is in good agreement with O1 and O2 detections, which suggest a dearth of merging BHs with mass $M_{\text{BH}} > 45 M_{\odot}$ (Abbott et al. 2018b).

The merger rate of BHs in the local Universe estimated from our models is $\sim 90 \text{ Gpc}^{-3} \text{ yr}^{-1}$, consistent with the BHB merger rate inferred from LIGO–Virgo data ($24 - 112 \text{ Gpc}^{-3} \text{ yr}^{-1}$, Abbott et al. 2018a,b)

Our results confirm that stellar winds, stellar radii and binary evolution processes (especially mass transfer and common envelope) are key ingredients to understand the statistics of merging BHs across cosmic time. Our new version of the SEVN code is uniquely suited to investigate this topic. In a follow-up paper we will consider stellar metallicity down to $Z \sim 10^{-7}$ and ZAMS masses up to $\sim 350 M_{\odot}$. The next step is to use SEVN in combination with *N*-body simulations to study the role of stellar dynamics on the formation and evolution of BHs.

ACKNOWLEDGEMENTS

We acknowledge the ‘‘Accordo Quadro INAF-CINECA (2017)’’ and the CINECA-INFN agreement for the availability of high performance computing resources and support. MS acknowledges funding from the European Union’s Horizon 2020 research and innovation programme under the Marie-Sklodowska-Curie grant agreement No. 794393. MM acknowledges financial support by the European Research Council for the ERC Consolidator grant DEMOBLACK, under contract no. 770017. AAT acknowledges support from JSPS KAKENHI Grant Number 17F17764. NG acknowledges financial support from Fondazione Ing. Aldo Gini and thanks the Institute for Astrophysics and Particle Physics of the University of Innsbruck for hosting him during the preparation of this paper. This work benefited from support by the International Space Science Institute (ISSI), Bern, Switzerland, through its International Team programme ref. no. 393 *The Evolution of Rich Stellar Populations & BH Binaries* (2017-18). MS thanks the Aspen Center for Physics, which is

supported by National Science Foundation grant PHY-1607611, where part of this work was performed.

REFERENCES

- Aasi J. et al., 2015, *Class. Quant. Grav.*, 32, 074001
 Abbott B. P. et al., 2016a, *Phys. Rev. X*, 6, 041015
 Abbott B. P. et al., 2016b, *Phys. Rev. Lett.*, 116, 061102
 Abbott B. P. et al., 2017a, *Phys. Rev. Lett.*, 118, 221101
 Abbott B. P. et al., 2017b, *Phys. Rev. Lett.*, 118, 221101
 Abbott B. P. et al., 2017c, *ApJ*, 851, L35
 Abbott B. P. et al., 2018a, preprint([arXiv:1811.12907](https://arxiv.org/abs/1811.12907))
 Abbott B. P. et al., 2018b, preprint([arXiv:1811.12940](https://arxiv.org/abs/1811.12940))
 Acernese F. et al., 2015, *Class. Quant. Grav.*, 32, 024001
 Askar A., Giersz M., Pych W., Olech A., Hypki A., 2016, in Meiron Y., Li S., Liu F.-K., Spurzem R., eds, IAU Symposium Vol. 312, Star Clusters and Black Holes in Galaxies across Cosmic Time. p. 262, preprint ([arXiv: 1501.00417](https://arxiv.org/abs/1501.00417))
 Askar A., Szkuldarek M., Gondek-Rosińska D., Giersz M., Bulik T., 2017, *MNRAS*, 464, L36
 Banerjee S., 2018, *MNRAS*, 473 909.
 Barrett J. W., Gaebel S. M., Neijssel C. J., Vigna-Gómez A., Stevenson S., Berry C. P. L., Farr W. M., Mandel I., 2018, *MNRAS*, 477, 4685,
 Belczynski K., Sadowski A., Rasio F. A., 2004, *ApJ*, 611, 1068
 Belczynski K., Kalogera V., Rasio F. A., Taam R. E., Zezas A., Bulik T., Maccarone T. J., Ivanova N., 2008, *ApJS*, 174, 223
 Belczynski K., Bulik T., Fryer C. L., Ruiter A., Valsecchi F., Vink J. S., Hurley J. R., 2010, *ApJ*, 714, 1217
 Belczynski K., Holz D. E., Bulik T., O'Shaughnessy R., 2016a, *Nature*, 534, 512
 Belczynski K. et al., 2016b, *A&A*, 594, A97
 Bethe H. A., Brown G. E., 1998, *ApJ*, 506, 780
 Bondi H., Hoyle F., 1944, *MNRAS*, 104, 273
 Bressan A., Marigo P., Girardi L., Salasnich B., Dal Cero C., Rubele S., Nanni A., 2012, *MNRAS*, 427, 127
 Carr B., Künnel F., Sandstad M., 2016, *Phys. Rev. D*, 94, 083504
 Chen Y., Bressan A., Girardi L., Marigo P., Kong X., Lanza A., 2015, *MNRAS*, 452, 1068
 Chen K.-J., Woosley S., Heger A., Almgren A., Whalen D. J., 2014, *ApJ*, 792, 28
 Chiosi C., Summa C., 1970, *Ap&SS*, 8, 478
 Colpi M., Mapelli M., Possenti A., 2003, *ApJ*, 599, 1260
 Cyburt R. H. et al., 2010, *ApJS*, 189, 240
 de Kool M., 1992, *A&A*, 261, 188
 de Mink S. E., Mandel I., 2016, *MNRAS*, 460, 3545
 Di Carlo U. N., Giacobbo N., Mapelli M., Pasquato M., Spera M., Wang L., Haardt F., 2019, preprint([arXiv:1901.00863](https://arxiv.org/abs/1901.00863))
 Dominik M., Belczynski K., Fryer C., Holz D. E., Berti E., Bulik T., Mandel I., O'Shaughnessy R., 2012, *ApJ*, 759, 52
 Eggleton P. P., 1983, *ApJ*, 268, 368
 Eldridge J. J., Stanway E. R., 2016, *MNRAS*, 462, 3302
 Eldridge J. J., Stanway E. R., Xiao L., McClelland L. A. S., Taylor G., Ng M., Greis S. M. L., Bray J. C., 2017, *PASA*, 34, e058
 Ertl T., Janka H.-T., Woosley S. E., Sukhbold T., Ugliano M., 2016, *ApJ*, 818, 124
 Farr W. M., Sravan N., Cantrell A., Kreidberg L., Bailyn C. D., Mandel I., Kalogera V., 2011, *ApJ*, 741, 103
 Foglizzo T. et al., 2015, *PASA*, 32, e009
 Fryer C. L., 1999, *ApJ*, 522, 413
 Fryer C. L., Woosley S. E., Heger A., 2001, *ApJ*, 550, 372
 Fryer C. L., Belczynski K., Wiktorowicz G., Dominik M., Kalogera V., Holz D. E., 2012, *ApJ*, 749, 91
 Fu X., Bressan A., Marigo P., Girardi L., Montalbán J., Chen Y., Nanni A., 2018, *MNRAS*, 476, 496
 Gallazzi A., Brinchmann J., Charlot S., White S. D. M., 2008, *MNRAS*, 383, 1439
 Gerosa D., Berti E., 2017, *Phys. Rev. D*, 95, 124046
 Giacobbo N., Mapelli M., 2018, *MNRAS*, 480, 2011
 Giacobbo N., Mapelli M., Spera M., 2018, *MNRAS*, 474, 2959
 Giersz M., Leigh N., Hypki A., Lützgendorf N., Askar A., 2015, *MNRAS*, 454, 3150
 Gräfener G., Hamann W.-R., 2008, *A&A*, 482, 945
 Heger A., Fryer C. L., Woosley S. E., Langer N., Hartmann D. H., 2003, *ApJ*, 591, 288
 Hobbs G., Lorimer D. R., Lyne A. G., Kramer M., 2005, *MNRAS*, 360, 974
 Hurley J. R., Pols O. R., Tout C. A., 2000, *MNRAS*, 315, 543
 Hurley J. R., Tout C. A., Pols O. R., 2002, *MNRAS*, 329, 8 97
 Hut P., 1981, *A&A*, 99, 126
 Ivanova N. et al., 2013, *A&A Rev.*, 21, 59
 Izzard R. G., Tout C. A., Karakas A. I., Pols O. R., 2004, *MNRAS*, 350, 407
 Izzard R. G., Dray L. M., Karakas A. I., Lugaro M., Tout C. A., 2006, *A&A*, 460, 565
 Izzard R. G., Glebbeek E., Stancliffe R. J., Pols O. R., 2009, *A&A*, 508, 1359
 Kimpton T. O., Spera M., Mapelli M., Ziosi B. M., 2016, *MNRAS*, 463, 2443
 Kroupa P., 2001, *MNRAS*, 322, 231
 Kruckow M. U., Tauris T. M., Langer N., Kramer M., Izzard R. G., 2018, *MNRAS*, 481, 1908,
 Kulkarni S. R., Hut P., McMillan S., 1993, *Nature*, 364, 421
 Laycock S. G. T., Maccarone T. J., Christodoulou D. M., 2015, *MNRAS*, 452, L31
 Limongi M., 2017, Supernovae from Massive Stars, Alsabti A.W. and Murdin P.in Handbook of Supernovae, Springer International Publishing AG, 513.
 Limongi M., Chieffi A., 2018, *ApJS*, 237, 13
 Madau P., Dickinson M., 2014, *ARA&A*, 52, 415
 Mandel I., de Mink S. E., 2016, *MNRAS*, 458, 2634
 Mapelli M., 2016, *MNRAS*, 459, 3432
 Mapelli M., Giacobbo N., 2018, *MNRAS*, 479, 4391
 Mapelli M., Zampieri L., 2014, *ApJ*, 794, 7
 Mapelli M., Colpi M., Zampieri L., 2009, *MNRAS*, 395, L71
 Mapelli M., Ripamonti E., Zampieri L., Colpi M., Bressan A., 2010, *MNRAS*, 408, 234
 Mapelli M., Zampieri L., Ripamonti E., Bressan A., 2013, *MNRAS*, 429, 2298
 Marchant P., Langer N., Podsiadlowski P., Tauris T. M., Moriya T. J., 2016, *A&A*, 588, A50
 Miyaji S., Nomoto K., Yokoi K., Sugimoto D., 1980, *PASJ*, 32, 303
 Nomoto K., 1984, *ApJ*, 277, 791
 Paxton B., Bildsten L., Dotter A., Herwig F., Lesaffre P., Timmes F., 2011, *ApJS*, 192, 3
 O'Connor E., Ott C. D., 2011, *ApJ*, 730,
 Özel F., Psaltis D., Narayan R., McClintock J. E., 2010, *ApJ*, 725, 1918
 Paxton B. et al., 2013, *ApJS*, 208, 4
 Paxton B. et al., 2015, *ApJS*, 220, 15
 Peters P. C., 1964, *Phys. Rev.*, 136, B1224
 Petit V. et al., 2017, *MNRAS*, 466, 1052
 Planck Collaboration et al., 2016, *A&A*, 594, A13
 Portegies Zwart S. F., McMillan S. L. W., 2000, *ApJ*, 528, L17
 Portegies Zwart S. F., Verbunt F., 1996, *A&A*, 309, 179
 Portegies Zwart S. F., Baumgardt H., Hut P., Makino J., McMillan S. L. W., 2004, *Nature*, 428, 724
 Prestwich A. H. et al., 2007, *ApJ*, 669, L21
 Rafelski M., Wolfe A. M., Prochaska J. X., Neeleman M., Mendez A. J., 2012, *ApJ*, 755, 89
 Rasio F. A., Tout C. A., Lubow S. H., Livio M., 1996, *ApJ*, 470, 1187
 Rodriguez C. L., Zevin M., Pankow C., Kalogera V., Rasio F. A., 2016, *ApJ*, 832, L2
 Sana H. et al., 2012, *Science*, 337, 444
 Sana H. et al., 2013, *A&A*, 550, A107
 Sasaki M., Suyama T., Tanaka T., Yokoyama S., 2018, *Classical and Quantum Gravity*, 35, 063001

- Schneider R., Graziani L., Marassi S., Spera M., Mapelli M., Alparone M., Bennassuti M. D., 2017, *MNRAS*, 471, L105
- Schutz B. F., 1989, in Hellings R. W., ed., NASA Conference Publication Vol. 3046. NASA Conference Publication
- Sigurdsson S., Phinney E. S., 1993, *ApJ*, 415, 631
- Silverman J. M., Filippenko A. V., 2008, *ApJ*, 678, L17
- Spera M., Mapelli M., 2017, *MNRAS*, 470, 4739
- Spera M., Mapelli M., Bressan A., 2015, *MNRAS*, 451, 4086
- Stevenson S., Berry C. P. L., Mandel I., 2017, *MNRAS*, 471, 2801
- Takahashi K., Yoshida T., Umeda H., 2013, *ApJ*, 771, 28
- Tang J., Bressan A., Rosenfield P., Slemer A., Marigo P., Girardi L., Bianchi L., 2014, *MNRAS*, 445, 4287
- Thorne K. S., 1987, *Science*, 236, 1007
- Toonen S., Nelemans G., Portegies Zwart S., 2012, *A&A*, 546, A70
- Tutukov A., Yungelson L., Klayman A., 1973, Nauchnye Informatsii, 27, 3
- Ugliano M., Janka H.-T., Marek A., Arcones A., 2012, *ApJ*, 757, 69
- Vink J. S., de Koter A., Lamers H. J. G. L. M., 2001, *A&A*, 369, 574
- Vink J. S., Muijres L. E., Anthonisse B., de Koter A., Gräfener G., Langer N., 2011, *A&A*, 531, A132
- Webbink R. F., 1984, *ApJ*, 277, 355
- Webbink R. F., 1985, Stellar Evolution and Binaries, Pringle, J. E. and Wade, R. A. in Interacting Binary Stars, Cambridge University Press, 39.
- Whyte C. A., Eggleton P. P., 1985, *MNRAS*, 214, 357
- Woosley S. E., 2017, *ApJ*, 836, 244
- Zahn J.-P., 1975, *A&A*, 41, 329
- Zahn J.-P., 1977, *A&A*, 57, 383
- Ziosi B. M., Mapelli M., Branchesi M., Tormen G., 2014, *MNRAS*, 441, 3703

SUPPORTING INFORMATION

Supplementary data are available at [MNRAS](#) online.

Appendix A. Interpolation.

Appendix B. Prescriptions for SNe.

Appendix C. Mass transfer.

Appendix D. Supplementary figures.

Please note: Oxford University Press is not responsible for the content or functionality of any supporting materials supplied by the authors. Any queries (other than missing material) should be directed to the corresponding author for the article.

This paper has been typeset from a TeX/LaTeX file prepared by the author.